Experimental comparison of solar methane pyrolysis in gas-phase and molten-tin bubbling tubular reactors

Malek Msheik, Sylvain Rodat, Stéphane Abanades

Experimental comparison of solar methane pyrolysis in gas-phase and molten-tin bubbling tubular reactors

Malek Msheik, Sylvain Rodat, Stéphane Abanades*

Processes, Materials and Solar Energy Laboratory, PROMES-CNRS, 7 Rue du Four Solaire, 66120 Font Romeu, France; malek.msheik@promes.cnrs.fr (M.M.); sylvain.rodat@promes.cnrs.fr (S.R.); stephane.abanades@promes.cnrs.fr (S.A.)

*Correspondence: stephane.abanades@promes.cnrs.fr; Tel.: +33-(0)4-68-30-77-30

Abstract

This study experimentally compares solar methane pyrolysis in gas phase and molten tin. Molten media are expected to facilitate carbon separation and to enhance solar-to-gas heat transfer. Effects of temperature (1000-1400°C), gas feed flow rate (0.5-1.0 NL/min), and methane molar fraction in the feed (0.1-0.5) on methane decomposition were investigated in a tubular solar reactor. Methane conversion in molten tin was significantly lower than in gas phase at all temperatures (e.g., 64% vs. 92% at 1300°C). It was justified by the negligible catalytic activity of tin, the small gas-liquid surface contact (bubble diameter ~5 mm) and reduced bubble-tin contact time, in comparison with gas-phase pyrolysis (e.g., 0.83 s vs. 0.5 s for 0.5 NL/min gas feed at 1300°C). For both routes, a temperature increase (1000-1400°C) improved methane conversion (gas phase: 2-98%, molten tin: 0-91%). Increasing feed flow rate (0.5-1.0 NL/min) decreased conversion (gas phase: 93-85%, molten tin: 64-48% at 1300°C) by reducing space-time in gas phase (0.83-0.42 s) or by inducing bubbles coalescence in molten tin. Increasing methane molar fraction in the feed generally decreased methane conversion but energy efficiencies were enhanced. The carbon produced in gas-phase pyrolysis was carbon black powder (50-100 nm) and carbon sheets in molten tin.

Keywords: Methane pyrolysis; Hydrogen production; Molten tin; Concentrated solar energy; Solar reactor; Solar fuels.

1 Introduction

The growth of energy consumption worldwide, especially CO_2-emitting fossil fuels (coal, diesel, gasoline, natural gas, etc.), has been exacerbating global warming. This fostered the research for sustainable and cleaner forms of energy to reduce greenhouse gas emissions [1]. Among alternative fuels, hydrogen is an environmentally benign gas highly demanded in several sectors with total consumption by application as follows: ammonia production (55%), oil refining (25%), methanol production (10%), others (<10%) such as public transport, food, welding, medicals, etc. [2].

Hydrogen does not naturally exist on Earth but has to be produced [3]. At industrial scale, total hydrogen production worldwide derives from various paths including steam reforming of

natural gas (48%), partial oxidation of hydrocarbons (30%), coal gasification (18%), or water splitting via electrolysis (4%) [4–8]. Except water splitting, all these processes emit CO/CO_2. However, electrolysis is still a high-cost technology unable to supplant low-cost, yet CO_2-emitting steam methane reforming (SMR) (3.19 €/kg H_2 for the cheapest water electrolysis using wind energy against 1.87 €/kg H_2 and 1.71 €/kg H_2 for SMR with and without CO_2 sequestration, respectively) [9,10].

Methane pyrolysis, also known as methane cracking, appears as a possible transition technology between cheap yet polluting SMR and green yet expensive water splitting. The chemical reaction of pyrolysis yields hydrogen with zero CO/CO_2 emissions (Eq. (1)). Moreover, the only byproduct besides hydrogen is solid carbon that could be of specific interest in the industry. Carbon market was estimated at about 15.5 billion dollars in 2020, mostly for tire and synthetic rubber manufacturing (>75%). In 2021, the carbon production was estimated as 13 million tons [11]. Carbon prices range from (i) premium carbon fibers (22-100 €/kg), (ii) high-value carbon nanotubes (0.1-530 €/kg) and graphite (9 €/kg), and (iii) less important or poor quality needle coke (1.5 €/kg) and carbon black (0.4-2 €/kg) [12]. Thus, premium and high-value carbons are desired to minimize hydrogen production costs through methane cracking. At lab scale, methane cracking for hydrogen production in molten media garnered specific attention recently, as it may offer several advantages over a gas-phase pyrolysis reaction. Indeed, molten metals and salts are expected to facilitate carbon separation (due to the density difference between solid carbon and liquids) and to enhance heat transfer in the reactor due to the bubbling regime. Therefore, a comparative assessment of methane pyrolysis in gas phase and molten media reactors is needed.

Methane cracking is an endothermic decarbonization reaction and thus, gas heating is required to provide the reaction enthalpy [13–16]. The heat source is important to maintain the green asset of methane pyrolysis. Concentrated solar energy (CSE) for solar-driven methane pyrolysis allows keeping the advantage of hydrogen production with zero CO_2 emissions. Furthermore, CSE seems worth investigating in methane cracking since high temperatures are easily reachable [17–20].

$$CH_{4(g)} \rightarrow 2H_{2(g)} + C_{(s)} \qquad \Delta H_{25\,^{\circ}C} = 74.85\ \text{kJ/mol of}\ CH_4 \qquad (1)$$

Over the last few decades, solid catalysts have been used to lower the activation energy of the reaction and to increase the reaction rate at moderate temperatures (below 1000°C). Such catalysts were either (i) metallic catalysts (Ni, Pd, Pt, Fe, Ni-Pd, etc.) usually supported on metal oxides (Al_2O_3, MgO, etc.) [21,22], or (ii) carbonaceous catalysts (activated char, carbon black, etc.) [23,24]. Though supports were used to increase both catalytic activity and lifetime of catalysts, the latter eventually deactivated due to carbon deposition on their surfaces. Moreover, carbon often stuck to the hot walls of the reactor and ultimately clogged it.

Pyrolysis in molten metals, instead of gaseous media, was also considered to favor carbon collection and improve heat transfer to the gas phase, aiming to enhance methane conversion. Bubbling methane in a hot molten metal/salt was first proposed in 1931 [25]. Herein, methane which is in contact with the hot liquid, decomposes while bubbles are rising. Hydrogen leaves with the outlet gas stream, while carbon should float atop the bath due to density difference. In short, such a technology allows a better heat transfer as liquids are better heat conductors than gases. Depending on the molten metal, catalytic effects can be obtained without issues of carbon deposition on the catalyst. The liquid phase also impedes reactor clogging caused by

carbon deposits on the hot walls. This alternative pathway is called molten media methane pyrolysis [26].

Among the most interesting results for pyrolysis in molten metals, Upham et al. [27] found that molten $Ni_{0.27}Bi_{0.73}$ alloy had the best catalytic activity among a wide variety of molten metals (In, Sn, Bi, Cu-Sn, etc.). Generally, a catalytic mechanism occurs at the gas-liquid interface while a gas-phase mechanism occurs toward the center of bubbles. The catalytic mechanism at the interface is not yet well-understood but assumed to be directly proportional to the surface area of bubbles [28]. Palmer et al. [29] discovered that $Cu_{0.45}Bi_{0.55}$ surpassed $Ni_{0.27}Bi_{0.73}$ performance, although Cu is much intrinsically weaker than Ni in terms of catalysis. This result proved that alloys may modify surface morphology so that weak catalysts may form alloys with high catalytic activity. Zeng et al. [30] reported that molten tellurium exceeded $Ni_{0.27}Bi_{0.73}$ performance. However, tellurium is a rare and very expensive metal. Leal Perez et al. [31] investigated methane pyrolysis in molten gallium. Although it was generally reported as a weak catalyst for methane decomposition, it led to 91% conversion at 1119°C because a 0.2 mm gas sparger was used to break methane bubbles into finer ones. Magnesium was also investigated by Wang et al. [32] to yield 30% methane conversion at only 700°C. However, Mg evaporates at 1090°C, complicating operations at high temperatures. Pure molten tin was also investigated [5,33–35], proving that bubble-liquid contact time highly impacted chemical conversion. Although molten tin is non-catalytic toward methane pyrolysis, its use permits the delineation of the transport phenomena in the two phases without the complications of catalytic activity.

Other significant studies concerning methane pyrolysis in molten media used salts as melts [36–39]. Kang et al. [36] studied pyrolysis in KCl, $MnCl_2$ (poor catalysts), and KCl/$MnCl_2$ mixtures with different molar percentages. They found that KCl(67 mol.%)/$MnCl_2$(33 mol.%) had the best performance with a conversion of 55% at 1050°C. Increasing $MnCl_2$ concentration lowered the activation energy. Kang et al. [37] studied the effect of Fe addition to NaKCl salt at 1000°C. They found that adding 3 wt.% Fe to NaKCl lowered activation energy from 301 to 171 kJ/mol and increased methane conversion from 4.5% to 9.5% at equilibrium. Parkinson et al. [38] conducted a study with four pure molten salts (NaBr, NaCl, KBr, and KCl) and a eutectic mixture of NaBr(48.7 mol.%)/KBr(51.3 mol.%). At 1000°C, KBr achieved the highest conversion of 6.22%. They also concluded that Na-containing salts led to purer carbon because Na has less adhesion energy toward carbon than K-containing salts. Generally, salts are usually less active than metals in terms of catalytic activity. However, purification of salt-contaminated carbon by salt dissolution in water is easier compared with metal-contaminated carbon.

Rahimi et al. [40] tested a two-phase mixture of molten metal (Ni-Bi) overlaid by a molten salt (KBr or NaBr). They reported a significant effect of salt presence on carbon purity: carbon product had 83 wt.% metal contamination in pure Ni-Bi vs. only 5 wt.% in Ni-Bi/KBr/NaBr because the salt phase condenses metal vapor and brings it back downwards due to density difference between metals and salts. Patzschke et al. [39] investigated various solid catalysts dispersed in molten NaBr(48.7 mol.%)/KBr(51.3 mol.%) salt. Co-Mn catalyst offered the best performance.

This work aims to experimentally investigate the difference between solar methane pyrolysis in a gaseous phase and a pure molten tin bath (non-catalytic metal). The impacts of

parameters like temperature, gas inlet volumetric flow rate, methane mole fraction in the inlet feed, and type of the reactional medium were discussed. The carbon separation issue was not addressed in the experiments that were chiefly dedicated to the analysis and comparison of thermochemical conversion performance in both configurations. Such a study aimed primarily to evaluate the effect of the liquid phase on methane conversion. It also highlighted the strong effect of key parameters such as diameter and rising time of bubbles that may suppress the benefits of molten metals for methane dissociation. The characteristics of produced solid carbon derived from both paths were also determined.

2 Process description

2.1 Solar reactor design

A solar reactor for methane cracking was designed and installed at PROMES-CNRS laboratory in Odeillo (France). The design was compatible with gas and liquid phase methane pyrolysis (Figure 1). It consisted of two coaxial tubes made of aluminum oxide (Al_2O_3) centered in a circular insulation layer to reduce heat losses with the external environment. The insulation was 7 cm thick, made of polycrystalline mullite/alumina wool (PCW) and special inorganic fibers and binders (commercially known as UltraBoard). Inner and outer tubes had lengths of 500 mm and 315 mm, inner diameters of 3 mm and 23 mm, and outer diameters of 6 mm and 30 mm, respectively. The outlet of the inner tube was held 10 mm above the bottom of the outer one to increase methane space-time in the reactor. The reactional zone was heated through a solar cavity receiver with a 15 mm diameter aperture. The cavity absorbed the concentrated solar flux received from a 1.5 kW heliostat-parabola solar system (2 m diameter parabolic dish with a peak concentration ratio of about 10000). The center of the solar cavity receiver was located 50 mm above the bottom of the reactor tube, so that a liquid bath of 120 mm height (in reference to the bottom of the outer tube) could be well heated as uniformly as possible. The zone of the molten metal was considered as the reaction zone.

Temperatures were measured by using four different thermocouples whose measuring tips were in direct contact with the outer wall of the outermost tube (Figure 1). The temperature indicator TI 1 (type S) measured the temperature at the bottom. TI 2 and TI 3 (both type S) were set respectively at the bottom and top of the solar cavity (their average value was thus used as the cavity temperature). To verify this approach, a fifth thermocouple TI 5 (type B) was inserted inside the tube where the tip was exactly at the solar cavity center. TI 4 (type K) measured the wall temperature of the effluent gas 50 mm above TI 3.

During a pyrolysis run, the inlet gas mixture (CH_4 + Ar) entered the inner tube from the top. Methane decomposition took place down in the hot zone. The gas then flowed up in the annular space between the two tubes and exited from the top after cooling. Water-cooling was only implemented to protect the gasket on top of the outer tube. The following section explains the implementation of the full process control.

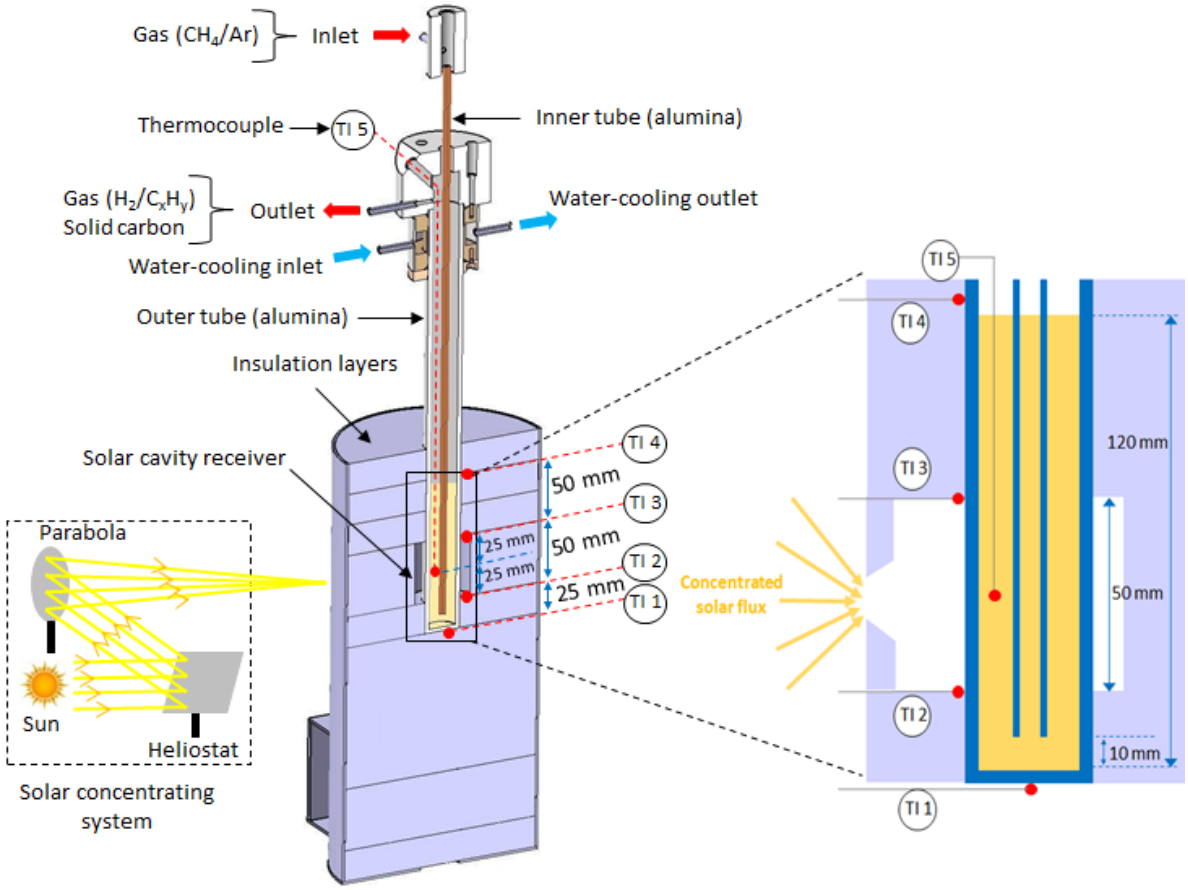

Figure 1: 3D sectional view of the methane cracking reactor designed and installed at PROMES-CNRS in Odeillo (France) and scheme of the solar cavity receiver.

2.2 Process control

Figure 2 illustrates the solar reactor integration in the whole process consisting of command and data acquisition. Both CH_4 and Ar gases were fed to the reactor through mass flow controllers (Brooks SLA5850S). Thus, the volumetric flow rate of each component, and hence the dilution ratio, could be fixed. The pressure of the diluted methane stream was continuously recorded with a pressure indicator (PI 1) (Keller Druckmesstechnik PAA-23, 0-3 bar). A pressure relief valve (Swagelok SS-RL3S6MM) was connected next to (PI 1) to purge gas if pressure surpasses safety levels (≈ 1.6 bar). Likewise, a pressure indicator (PI 2) and a pressure relief valve were set just after the reactor exit to record and control pressure values.

After methane decomposition in the reactor, the outlet mixture was sent to two cartridge gas filters (Classic filters SG231.221, 0.1 µm particles removal) in series to separate and capture the entrained solid carbon particles. Possible remaining carbon traces could be removed through a water bubbler placed downstream of the second filter. The clean gas was then fed to an online gas analyzer (Rosemount NGA 2000 MLT3) for measuring CH_4 and H_2 concentrations, and to a gas chromatograph GC (Varian CP 4900, equipped with two channels: MolSieve 5 Å PLOT for H_2 and CH_4, PoraPLOT U for H_2, CH_4, and C_2H_y).

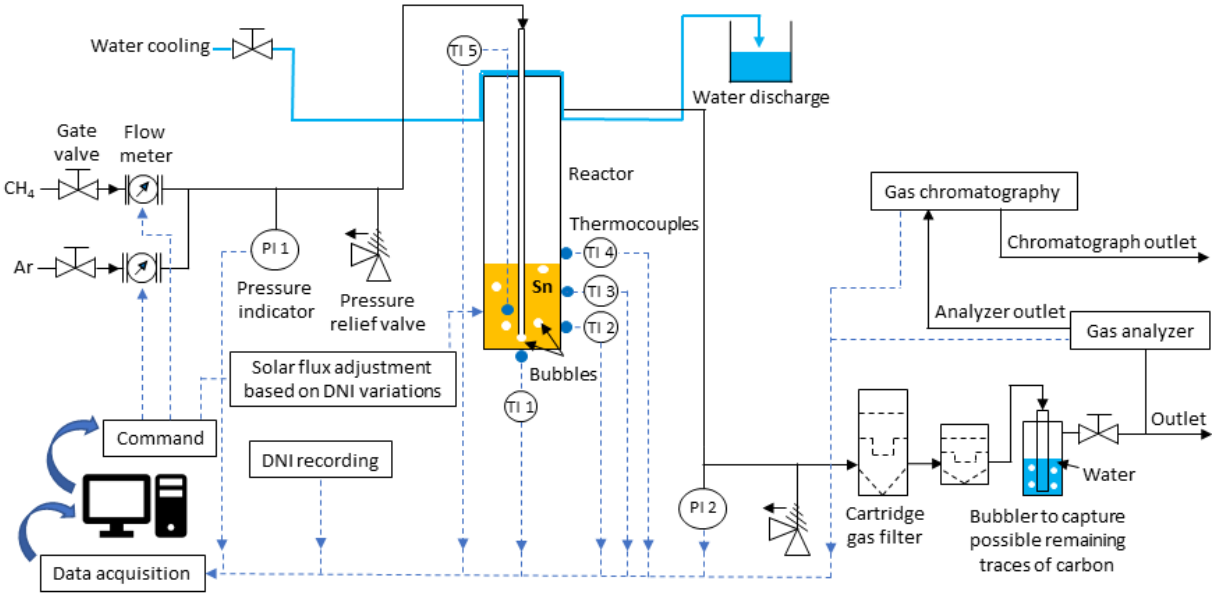

Figure 2: Scheme of the flowsheet representing the process control.

3 Materials and Methods

Gases were CH_4 (purity > 99.9%) and Ar (purity > 99.99%) both provided by Air Liquide (France). Tin metal was selected as the molten medium based on its suitable physical properties, which were compatible with methane cracking conducted at temperatures typically ranging from 1000 to 1400°C. Melting and boiling temperatures (232°C and 2602°C, respectively [26]) are important in a pyrolysis process in bubble columns.

The height of the tin bath in the reactor was set to 120 mm as bubbling was expected to homogenize the temperature in this zone. Liquid tin density varies as a function of temperature. Based on the mass conservation of tin, the required quantity was calculated using Eq. (2) [41]. Consequently, 308 g of solid tin in the form of granules (Figure 3) were weighed to form a liquid bath of 120 mm height at 1000°C. They were inserted progressively in the reactor during heating to warrant uniform metal melting.

$$\rho_{Sn} = 7.309 - 6.127 \times 10^{-4}\,(T + 273.15) \qquad (2)$$

where ρ_{Sn} is liquid tin density (g/cm^3) and T is the operating temperature (°C).

Figure 3: Granules of solid tin to be inserted in the reactor.

This work aimed to investigate the difference between methane pyrolysis in gas phase (empty tube) and molten tin. For both routes, the effects of parameters like (i) temperature, (ii)

methane mole fraction in the feed, (iii) inlet volumetric flow rate, and (iv) space-time were studied. The comparison was mainly based on methane conversion and products yield.

For this purpose, two configurations were considered: the first was uncatalyzed gas-phase pyrolysis and the second was pyrolysis in molten tin (Table 1). In each case, the parameters to be studied were changed to investigate their effect on methane conversion. Temperature was studied between 1000 and 1400°C. Three methane molar fractions in the inlet stream were used (0.1-0.3-0.5). At an inlet methane molar fraction of 0.3 and a constant temperature of 1300°C, the total inlet flow rate was studied with three different values (0.5-0.75-1 NL/min). In total, 33 experimental runs were achieved, as shown in Table 1. Q_0 was the total volumetric flow rate of the feed (CH_4+Ar) and $y_{0,CH4}$ was the inlet methane mole fraction. T was the operating temperature in the reactor calculated as the average of TI 2 and TI 3.

Table 1: Summary of the methane cracking runs in gas-phase and in molten tin

Run#	Medium type	Q_0 (NL/min)	$y_{0,CH4}$	T (°C)
1	Gas phase	0.5	0.1	1000
2	Gas phase	0.5	0.3	1000
3	Gas phase	0.5	0.5	1000
4	Gas phase	0.5	0.1	1100
5	Gas phase	0.5	0.3	1100
6	Gas phase	0.5	0.5	1100
7	Gas phase	0.5	0.1	1200
8	Gas phase	0.5	0.3	1200
9	Gas phase	0.5	0.5	1200
10	Gas phase	0.5	0.1	1300
11	Gas phase	0.5	0.3	1300
12	Gas phase	0.5	0.5	1300
13	Gas phase	0.75	0.3	1300
14	Gas phase	1	0.3	1300
15	Gas phase	0.5	0.3	1300
16	Gas phase	0.5	0.1	1400
17	Gas phase	0.5	0.3	1400
18	Gas phase	0.5	0.5	1400
19	Molten tin	0.5	0.1	1000
20	Molten tin	0.5	0.1	1100
21	Molten tin	0.5	0.3	1100
22	Molten tin	0.5	0.5	1100
23	Molten tin	0.5	0.1	1200
24	Molten tin	0.5	0.3	1200
25	Molten tin	0.5	0.5	1200
26	Molten tin	0.5	0.1	1300
27	Molten tin	0.5	0.3	1300
28	Molten tin	0.5	0.5	1300
29	Molten tin	0.75	0.3	1300
30	Molten tin	1	0.3	1300
31	Molten tin	0.5	0.1	1400
32	Molten tin	0.5	0.3	1400
33	Molten tin	0.5	0.5	1400

TI5 was inserted in the gas-phase configuration to compare the temperatures inside the reactor and on its external walls (TI 5 vs. TI 2 and TI 3).

The average temperature of TI 2 and TI 3 was calculated and denoted as TI av. The difference between TI av and TI 5 (ΔT) was then calculated (Figure 4). At 1000°C and 1100°C, ΔT was almost 0°C at thermal equilibrium. At 1200°C and 1300°C, ΔT varied between 15 and 25°C. This was mainly because thermal equilibrium was not yet reached above 1200°C. However, TI av and TI 5 remained close. For liquid phase pyrolysis, ΔT should be even lower since liquid tin has better thermal conductivity than gas, enabling homogeneous heating of the reaction zone.

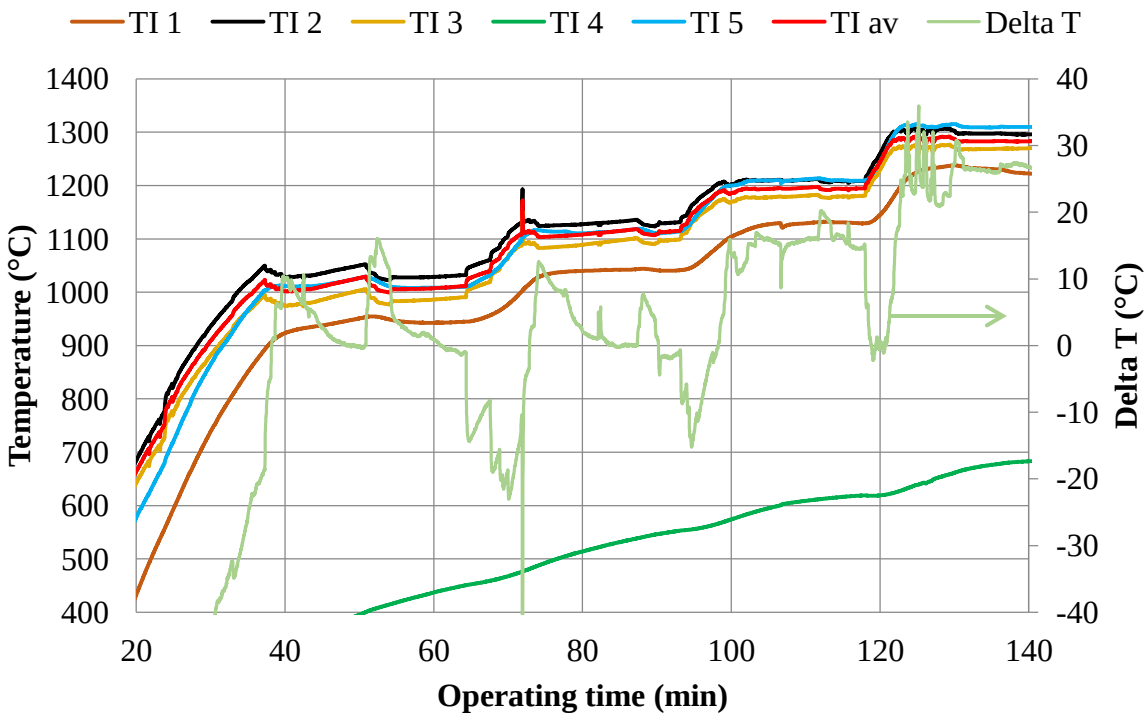

Figure 4: Temperature measurements in run #1-15 (gas-phase pyrolysis).

Calculation of methane conversion and products yield

Methane conversion was calculated as follows:

$$X_{CH_4} = 1 - \frac{y_{CH_4} . F_t}{F_{0,CH_4}} \quad (3)$$

where X_{CH4} is methane conversion, y_{CH4} is outlet methane molar fraction, F_t is total outlet molar flow rate (mol/min), and $F_{0,CH4}$ is methane inlet molar flow rate (mol/min). The total outlet molar flow rate F_t was calculated as follows:

$$F_t = \frac{F_{Ar}}{1 - y_{H_2} - \sum y_{C_xH_y}} \quad (4)$$

where F_{Ar} is argon molar flow rate (mol/min), y_{H2} is outlet molar fraction of hydrogen and y_{CxHy} is outlet molar fraction of hydrocarbons (CH_4, C_2H_2, C_2H_4 and C_2H_6).

Hydrogen yield was obtained through the following expression:

$$Y_{H_2} = \frac{y_{H_2} . F_t}{2\, F_{0,CH_4}} \tag{5}$$

Carbon yield was calculated as:

$$Y_C = 1 - \frac{\sum x . y_{C_xH_y} . F_t}{F_{0,CH_4}} \tag{6}$$

where x is the carbon stoichiometry in the molecular formula of the hydrocarbon (x=1 for CH_4 and x=2 for C_2H_2, C_2H_4 and C_2H_6).

Calculation of space-time

Space-time of the gas was an important parameter that influenced chemical conversion. In gas-phase pyrolysis, it was directly related to the inlet volumetric flow rate Q_0 (Eq. (7)). To calculate the space-time of the feed in gas-phase pyrolysis, the following expression can be applied:

$$\tau_g = \frac{V_r}{Q_0 . \beta} = \frac{V_r}{Q_0 \frac{P_0 . (T + 273)}{P . (T_0 + 273)}} \tag{7}$$

where τ_g is the gas effective space-time in the reactor (s), V_r is the effective volume of the reactor (i.e., the volume of the hot part of the reactor where CH_4 decomposition occurs) assumed to be equivalent to the liquid volume (120 mm height) in molten-tin pyrolysis ($47x10^{-6}$ m^3), β is the thermal expansion factor, P_0 and T_0 are the normal conditions (101325 Pa, 0 °C), and P (Pa) and T (°C) are the operating pressure and temperature.

In contrast, in liquid media, the bubble rising velocity did not significantly depend on the inlet flow rate (Eqs. (8), (9) and (10)). It was only related to the medium properties (viscosity, density, etc.), the bubble size, and of course, the liquid height as well. However, the inlet flow rate affected the bubble formation time, which can play an important role in bubble preheating (if it is long enough). Another possible phenomenon that may arise from inlet flow rate variations in molten media was coalescence of bubbles. When two bubbles coalesced, they formed a bigger bubble that rose faster than a smaller one.

To calculate space-time of gas bubbles in the reactor, their size should be calculated beforehand using Tate's law [42]:

$$D_b = \left(\frac{12 R_0 . \sigma}{(\rho_l - \rho_g) . g} \right)^{\frac{1}{3}} \tag{8}$$

where D_b is the bubble diameter (m), R_0 is the feeder radius (inner radius of the inner tube (m)), σ is the surface tension of the tin bath (N/m), ρ_l is the tin density (kg/m^3) and g is the gravitational acceleration constant (g = 9.8 m/s^2). ρ_g is the gas (methane + argon) density (kg/m^3) which could be neglected compared with tin density.

Tin surface tension and density were dependent on temperature. As a recall, tin density equation was provided previously in Eq. (2). Tin surface tension was calculated through the following equation [43]:

$$\sigma_{Sn} = \frac{580 - 0.065\ (T + 273)}{1000} \tag{9}$$

where T is the operating temperature (°C) and σ_{Sn} is the tin surface tension (N/m).

Once D_b is calculated, it is possible to estimate the bubble rising velocity in the liquid tin bath. The following expression is an empirical equation for a laminar flow of bubbles injected in a molten tin bath [44]:

$$u_b = 29.69\ D_b^{0.316} \tag{10}$$

where u_b is the bubble rising velocity (cm/s). D_b should be converted to cm in Eq. (10).

Finally, the bubble rising time was calculated using Eq. (11).

$$\tau'_l = \frac{H_{bath}}{u_b} \tag{11}$$

where H_{bath} is the height of the liquid bath inside the reactor (cm).

A bubble formation time was calculated using Eq. (12), which is actually the inverse of bubbles generation rate:

$$\tau_{formation} = \frac{V_b}{Q_0} \tag{12}$$

where V_b is the bubble volume (m^3).

The total space-time of the gas in the liquid phase is the sum of the bubbles formation time and their rising time. Consequently, the total gas space-time in the liquid bath is represented by Eq. (13):

$$\tau_l = \frac{V_b}{Q_0} + \frac{H_{bath}}{u_b} \tag{13}$$

Solar-to-fuel and thermal efficiency assessment

Solar-to-fuel efficiency is the ratio of the higher heating value of products to the sum of the input solar power absorbed by the reactor and the higher heating value of the methane feed [45]:

$$\eta_{SF} = \frac{\sum F_i . HHV_i}{P_{solar} + F_{0,CH_4} . HHV_{CH_4}} \tag{14}$$

where F_i is the outlet molar flow rate of component i (mol/s) and HHV_i is the higher heating value of the products (J/mol) (H_2, C_2H_2, C_2H_4, C_2H_6 and solid carbon). P_{solar} is solar power input (W).

Higher heating values for the different reaction components, given in Table 2, can be extracted from Cantera [46].

Table 2: Higher heating values of the different compounds of the pyrolysis reaction

Component	H_2	CH_4	C_2H_2	C_2H_4	C_2H_6	$C_{(s)}$
HHV (J/mol)	141777	55510	49967	50302	51900	32800

Reactor thermal efficiency was calculated using Eq. (15) [47], without considering Ar heating:

$$\eta_{thermal} = \frac{F_{0,CH_4}.(1 - X_{CH_4}).\int_{298}^{T} C_{p,CH_4}.dT + F_{0,CH_4}.X_{CH_4}.\Delta H^0_{298\,K} + 2F_{H_2}.\int_{298}^{T} C_{p,H_2}.dT + F_C.\int_{298}^{T} C_{p,C}.dT}{P_{solar}} \quad (15)$$

where F_{H2} and F_C are the hydrogen and carbon outlet molar flow rates, respectively, $\Delta H^{\circ}_{298\,K}$ is the reaction enthalpy at 298 K (74850 J/mol of CH_4) and C_p is the specific heat of species i ($J.mol^{-1}.K^{-1}$) (function of temperature) following Eq. (16):

$$C_{p,i} = (A + B.T + C.T^2 + D.T^3 + E.T^4).10^{-3}.M_i \quad (16)$$

where A, B, C, D and E are constants given in Table 3 [48], M_i is the molecular weight of species i (g/mol), and T is the operating temperature (K).

Table 3: Constants of specific heat expressions function of temperature

Species	A	B	C	D	E	M_i (g/mol)
CH_4	936.17117	4.24316	-0.00015466	-5.69283E-07	1.30084E-10	16
H_2	14842.4718	-2.6202	0.0047	-2.02117E-06	3E-10	2
C	-432.85513	4.88985	-0.00386	1.39948E-06	-1.89099E-10	12

Reaction rate

Methane pyrolysis is generally assumed as a first order chemical reaction, directly proportional to methane concentration [49]. Thus, the reaction rate can be represented as follows, assuming it follows an Arrhenius law:

$$r = k.[CH_4]_t = A.e^{-\frac{E_a}{R.T}}.[CH_4]_t \quad (17)$$

where r is the reaction rate, k is the kinetic constant, A is the pre-exponential factor (s^{-1}), E_a is the activation energy (J/mol), and T is the operating temperature (K).

Assuming a plug flow reactor (PFR), k can be calculated as follows [13,50]:

$$k = \frac{-\beta.(1 + \alpha).\ln(1 - X_{CH_4}) - \alpha.\beta.X_{CH_4}}{\tau} \quad (18)$$

Where α is the chemical expansion factor and τ is the gas (methane + argon) space-time.

To calculate the activation energy and the pre-exponential factor, ln(k) should be represented as a function of (1/RT) for a temperature range, known as Arrhenius plot in Eq. (19):

$$\ln(k) = -\frac{E_a}{R.T} + \ln(A) \quad (19)$$

4 Results and discussion

Results of methane pyrolysis runs, for both gas phase and molten tin are given in Table 4.

Table 4: Results of methane pyrolysis runs

Run#	Medium type	T (°C)	yH_2	yCH_4	yC_2H_2 (ppm)	yC_2H_4 (ppm)	yC_2H_6 (ppm)	X_{CH4} (%)	Y_{H2} (%)	Y_C (%)	η_{SF} (%)	$\eta_{thermal}$ (%)
1	Gas phase	1000	0.00	0.10	0	172	63	1	1	0	0.0	0.4
2	Gas phase	1000	0.00	0.30	238	1190	270	2	0	1	0.2	1.1
3	Gas phase	1000	0.01	0.49	240	2097	776	3	1	2	0.4	1.8
4	Gas phase	1100	0.04	0.07	1470	782	50	24	22	20	0.5	0.5
5	Gas phase	1100	0.15	0.19	6899	4574	335	32	26	24	1.9	1.5
6	Gas phase	1100	0.24	0.31	12342	9871	951	30	27	19	2.9	2.6
7	Gas phase	1200	0.13	0.03	5274	1175	33	72	70	58	1.3	0.8
8	Gas phase	1200	0.33	0.07	12460	5588	147	71	66	57	3.6	2.3
9	Gas phase	1200	0.49	0.11	14494	8563	274	71	65	58	5.5	3.8
10	Gas phase	1300	0.17	0.00	4999	1086	22	95	93	81	1.5	0.9
11	Gas phase	1300	0.42	0.02	8698	4207	108	92	88	81	4.0	2.6
12	Gas phase	1300	0.61	0.03	10001	6717	246	91	89	81	6.2	4.4
13	Gas phase	1300	0.41	0.02	7258	3333	75	90	86	81	5.6	3.9
14	Gas phase	1300	0.39	0.04	10995	3914	70	85	82	72	6.9	5.0
15	Gas phase	1300	0.42	0.02	7411	3099	73	93	89	84	4.0	2.6
16	Gas phase	1400	0.18	0.00	1620	570	93	99	98	94	1.3	0.9
17	Gas phase	1400	0.45	0.00	2442	922	25	98	97	95	3.5	2.5
18	Gas phase	1400	0.65	0.01	2538	1323	34	98	97	95	5.5	4.3
19	Molten tin	1000	0.00	0.10	0	21.8	27.3	0	0	0	0.0	0.2
20	Molten tin	1100	0.00	0.10	0	204	189	2	1	1	0.0	0.3
21	Molten tin	1100	0.01	0.29	61	2273	1036	3	1	1	0.2	0.7
22	Molten tin	1100	0.01	0.49	194	1564	0	1	1	0	0.1	1.2
23	Molten tin	1200	0.03	0.08	709	764	141	17	16	13	0.2	0.4
24	Molten tin	1200	0.11	0.22	4651	3761	247	22	19	15	1.0	1.1
25	Molten tin	1200	0.18	0.35	9412	7758	464	21	20	14	1.6	1.8
26	Molten tin	1300	0.12	0.03	4456	1131	83	65	63	53	0.9	0.6
27	Molten tin	1300	0.31	0.09	10256	3923	86	64	61	53	2.5	1.8
28	Molten tin	1300	0.47	0.14	14661	7384	193	64	62	52	4.0	3.0
29	Molten tin	1300	0.26	0.12	13408	4363	103	54	50	40	3.2	2.4
30	Molten tin	1300	0.24	0.14	15470	4893	146	48	46	32	3.8	3.1
31	Molten tin	1400	0.17	0.01	4705	817	22	93	91	80	1.0	0.7
32	Molten tin	1400	0.42	0.02	6407	2359	46	91	88	84	2.8	2.0
33	Molten tin	1400	0.61	0.04	9487	5451	159	90	88	81	4.5	3.3

4.1 Effect of temperature

Figure 5 displays CH_4 and H_2 mole fractions in the outlet stream. CH_4 mole fraction significantly decreased with increasing temperature, while H_2 mole fraction increased. The same behavior was observed in both pyrolysis configurations. For instance, in gas-phase pyrolysis, CH_4 mole fraction decreased from 0.3 at 1000°C to almost 0 at 1400°C for an inlet

CH_4 mole fraction of 0.3. For the same temperature change and the same feed, H_2 mole fraction increased from 0 to 0.45.

Mole fractions of secondary hydrocarbons rose with temperature to reach a maximum and then decreased at relatively high temperatures (Figure 6). C_2H_2 mole fraction reached its maximum at 1200°C for gas phase (14494 ppm) and at 1300°C for molten tin (14661 ppm), both for 0.5 inlet CH_4 fraction. C_2H_4 reached its maximum at 1100°C for gas phase (9871 ppm) and at 1200°C for molten tin (7758 ppm), both for 0.5 inlet CH_4 fraction. C_2H_6 was below ~1000 ppm, whatever the conditions. It can be concluded from these values that the most produced hydrocarbon was C_2H_2 followed by C_2H_4 then C_2H_6.

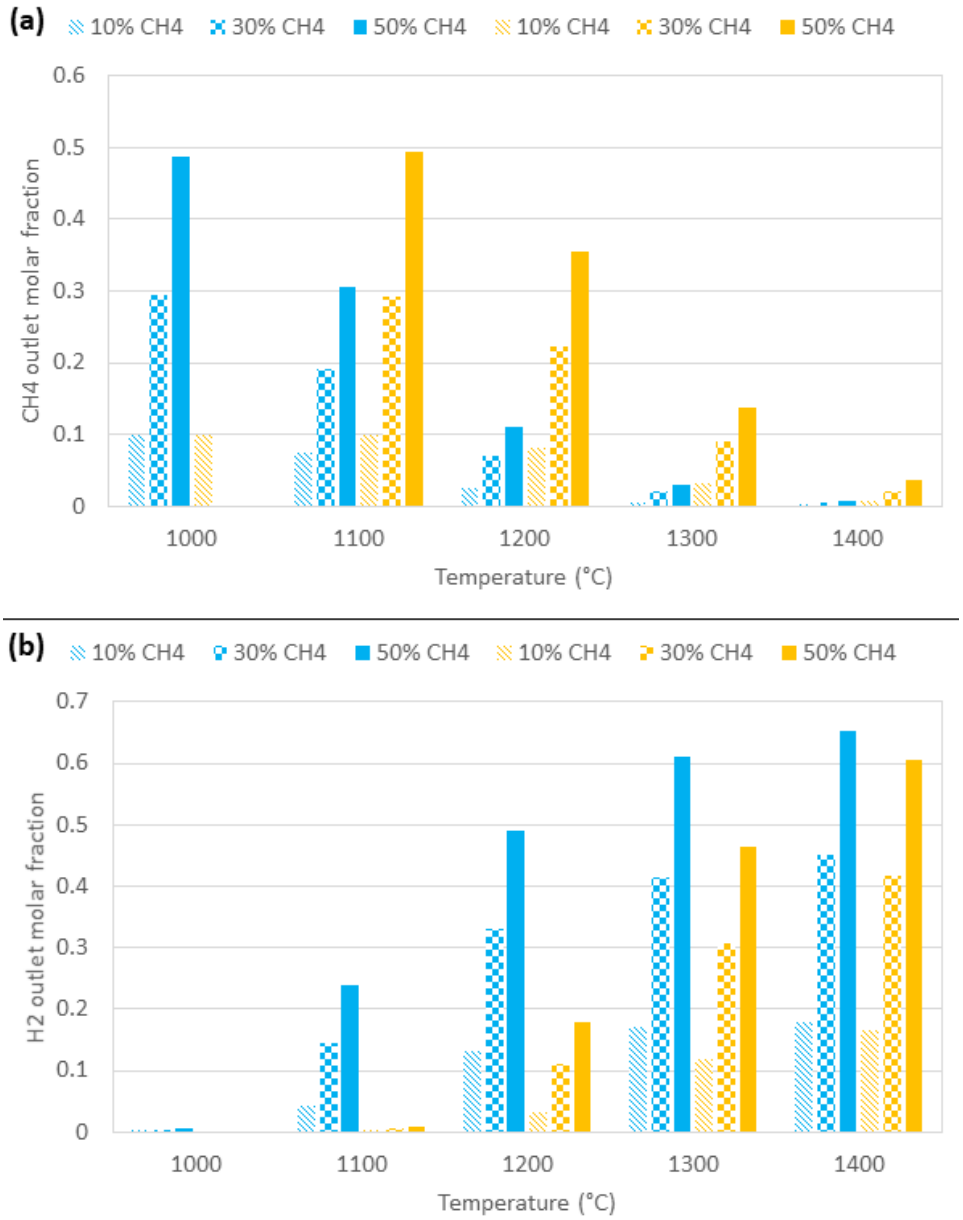

Figure 5: Effect of temperature on (a) CH_4 and (b) H_2 molar fractions for gas-phase pyrolysis (blue color) and liquid-tin pyrolysis (orange color).

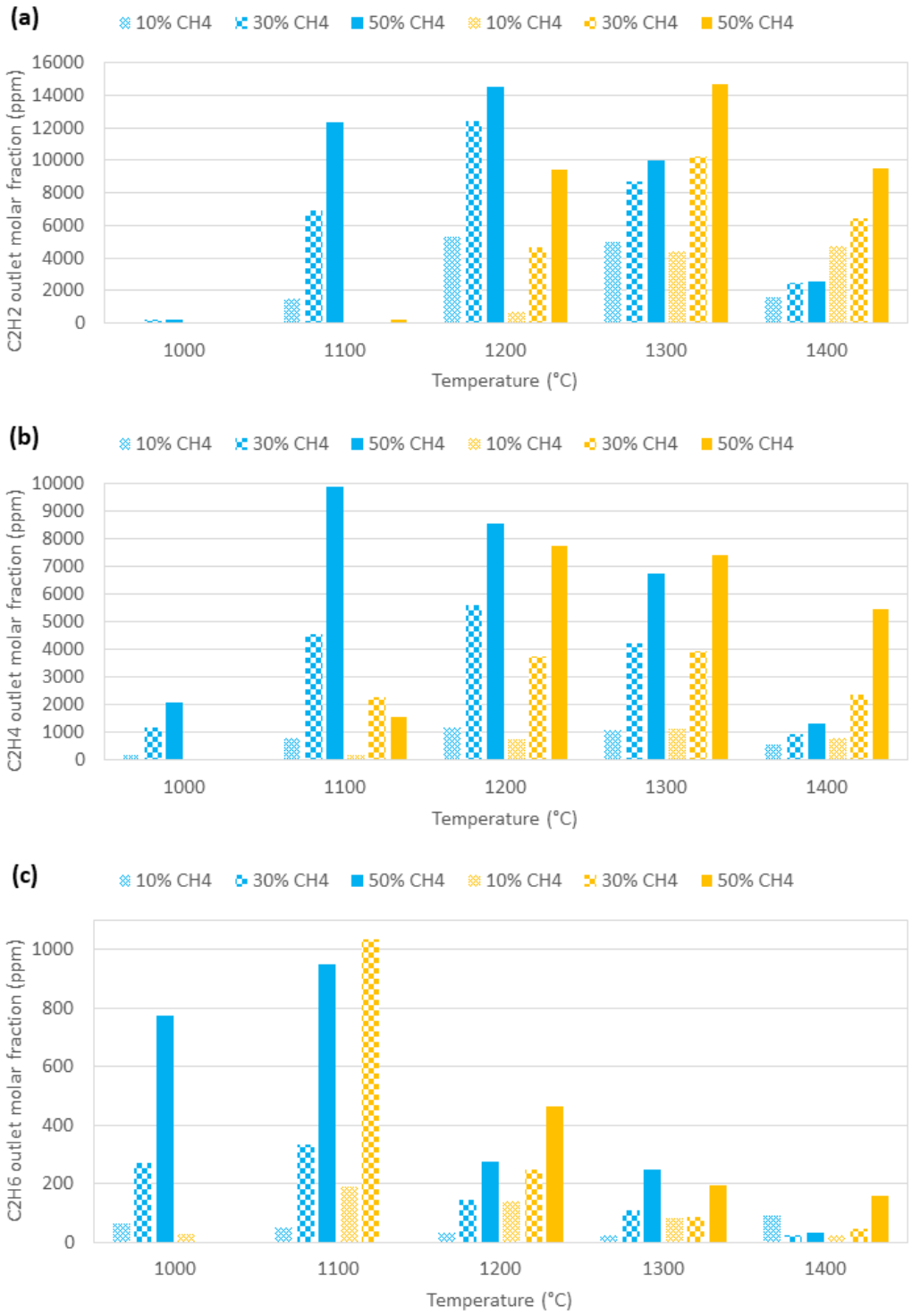

Figure 6: Effect of temperature on (a) C_2H_2 (b) C_2H_4 and (c) C_2H_6 molar fractions for gas-phase pyrolysis (blue color) and liquid-tin pyrolysis (orange color).

The effect of temperature on methane pyrolysis performance was studied. Runs with a fixed total inlet flow rate Q_0 (0.5 NL/min) and methane inlet molar fraction (0.3) were compared (gas phase: runs #2-5-8-11-17, molten tin: runs #19-21-24-27-32).

Figure 7 shows the tendency of methane conversion, hydrogen and carbon yields as a function of the operating temperature. Increasing the temperature resulted in both higher conversion

and products yield. When T was increased from 1000°C to 1400°C, CH_4 conversion in gas-phase pyrolysis increased from 2% to 98%, and hydrogen and carbon yields increased from 0 to 97% and from 1% to 95%, respectively. Within the same temperature range, the same behavior was observed for pyrolysis in molten tin: CH_4 conversion increased from 0% to 91%, hydrogen yield increased from 0% to 88%, and carbon yield increased from 0% to 84%.

These results were expected since methane pyrolysis is an endothermic reaction that requires external heat. Therefore, raising the operating temperature favored the reaction (Eq. (1)), leading to higher chemical conversion and products yield.

However, one could notice that methane conversion in molten tin was significantly lower than in gas-phase pyrolysis for each temperature. At 1200°C, the difference in methane conversion was significant: 71% vs. 22% for pyrolysis in gas phase and molten tin, respectively. However, this conversion difference decreased at higher temperatures (1400°C) because decomposition was enhanced (98% vs. 91% for gas-phase and molten-tin pyrolysis, respectively). The difference in conversion could be attributed to several parameters like space-time and bubble size in molten tin affecting both liquid/gas contact time and interface area, thus ultimately impacting liquid-to-gas heat transfer (as detailed in the next section). The lower conversion in molten tin was explained by the fact that the space-time of rising bubbles was significantly lower than that in the gas-phase pyrolysis. Moreover, the generation of relatively large bubbles cancelled the benefits of the liquid phase in terms of heat transfer. Decreasing the bubble size is thus recommended to improve the conversion. The easier downstream carbon separation in the molten-metal case can still outweigh the lower thermochemical performance observed in the reaction zone.

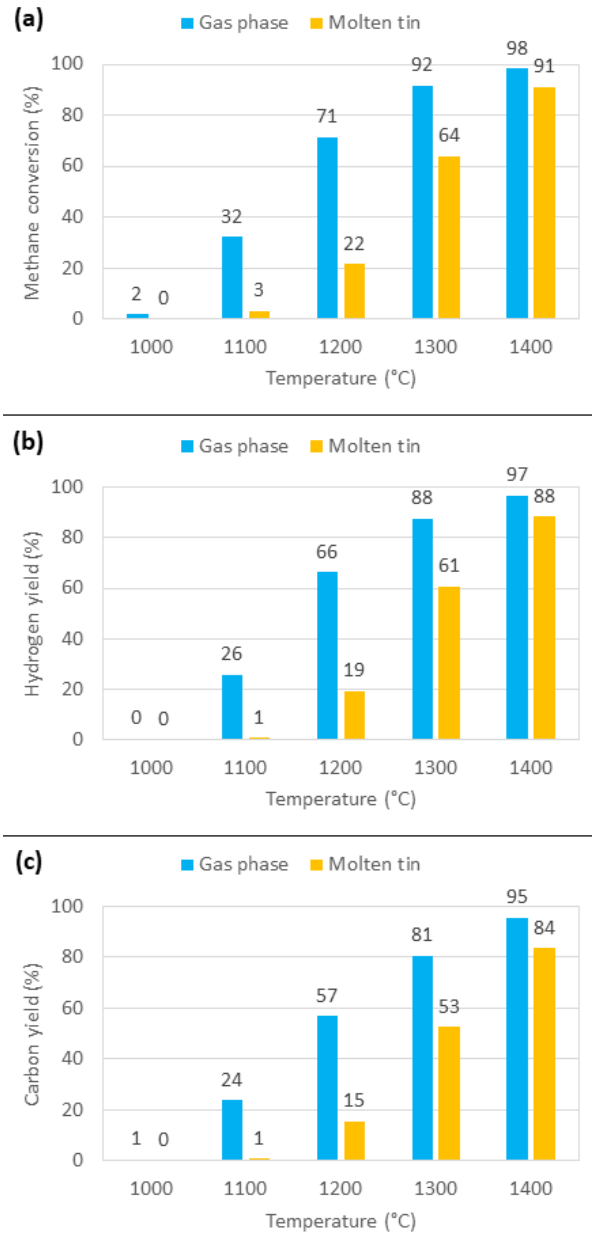

Figure 7: Temperature effect on methane pyrolysis in gas phase and in liquid tin for a fixed inlet flow rate of 0.5 NL/min with a fixed initial methane molar fraction of 0.3: (a) methane conversion, (b) hydrogen yield, (c) carbon yield.

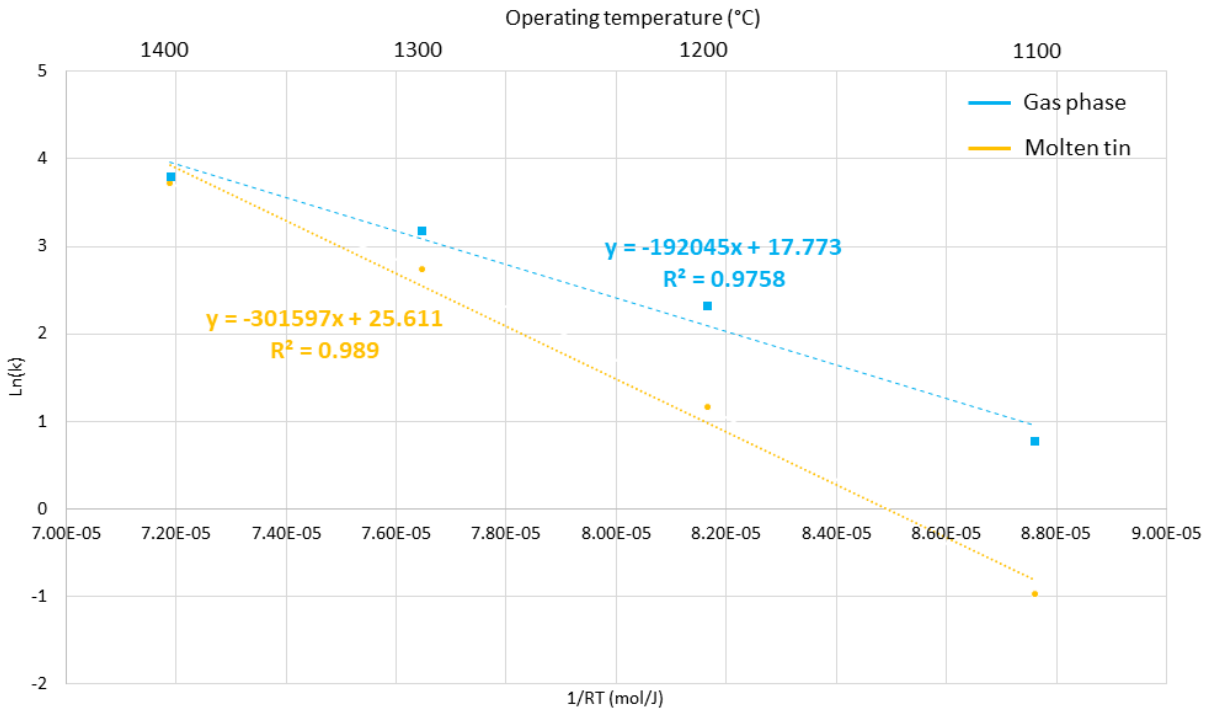

Figure 8: Arrhenius plots for methane pyrolysis in gas phase and in molten tin with a fixed inlet rate of 0.5 NL/min and a fixed methane inlet fraction of 0.3.

Figure 8 plots the reaction rate between 1100 and 1400°C. Below these temperatures, the conversion was weak because of slow reaction rates. The activation energy for molten tin was estimated as E_a = 302 kJ/mol with a pre-exponential factor A = 1.3 x 10^{11} s^{-1}. The only study that reported activation energy and pre-exponential factor for methane pyrolysis in pure molten tin was that of Zaghloul et al. [35] (E_a = 204.6 kJ/mol, A = 3.3 x 10^7 s^{-1}). For gas-phase pyrolysis, the kinetic parameters were E_a = 192 kJ/mol and A = 5.23 x 10^7 s^{-1}, where E_a is lower than values reported in literature for uncatalyzed gas-phase methane pyrolysis (356<E_a<450 kJ/mol) [14,19,51–53]. Such a low value of E_a in gas phase could be partially explained by the carbon byproduct deposit inside the reactor that could have some catalytic activity.

4.2 Effects of inlet gas flow rate and residence time

The inlet gas flow rate was a critical factor influencing methane decomposition. It indeed affected the space-time of methane molecules in the reactor (especially for gas-phase pyrolysis), and hence the methane conversion and products yield. To study the effect of inlet flow rate on methane decomposition, runs with a fixed methane molar fraction (0.3) at 1300°C were compared (gas phase: runs #13-14-15, molten tin: runs #27-29-30). In these runs, the only variable was the total inlet flow rate studied at three different values (0.5-0.75-1 NL/min). Results are shown in Figure 9. For both pyrolysis pathways, methane conversion and products yield decreased when increasing the flow rate. Using Eqs. (7) and (13), the space-time of the gas (CH_4+Ar) was calculated.

In gas-phase pyrolysis, when the inlet flow rate was doubled (from 0.5 to 1 NL/min), the space-time decreased from 0.83 to 0.42 s. Consequently, methane conversion decreased from 93% to 85%, hydrogen yield decreased from 89% to 82%, and carbon yield decreased from 84% to 72%. This result was expected as Eq. (7) reflected the direct relation between residence time and inlet feed flow rate.

Regarding pyrolysis in molten tin, Eq. (13) shows that the feed inlet rate only affected bubbles formation time. Once bubbles detached from the gas feeder, their rising velocity depended on the medium properties (density, viscosity, temperature). Calculations revealed a bubble diameter of 5.17 mm using Eq. (8), and thus a formation time of 0.008 s at 0.5 NL/min, decreasing to 0.004 s at 1 NL/min using Eq. (12). The rising time, independent of Q_0, was 0.5 s calculated using Eq. (11). This would be true only if no coalescence occurred at such feed rates. Globally, the total gas space-time was considered to be the rising time since the bubbles formation time was negligible. Although space-time in molten tin was theoretically constant when the inlet flow rate was doubled, methane conversion, hydrogen and carbon yields decreased from 64% to 48%, 61% to 46%, and 53% to 32%, respectively. Thus, there was most probably a coalescence phenomenon significantly impacting the rising velocity of bubbles. When bubbles coalesced, they formed bigger ones. According to Eq. (10), when the bubble diameter increased, the rising velocity increased as well, which reduced the gas space-time (i.e. the liquid/gas contact time) in the hot tin bath, thus explaining the lower methane conversion.

In order to obtain a bubble-tin contact time of 0.83 s in molten tin similar to the space-time in gas phase at 0.5 NL/min, the bubble diameter should not exceed 1 mm (Eq. 11). In this case, the gas-liquid interfacial area would be increased by a factor of 5.2. This bubble size reduction would increase the space-time of rising bubbles, while enhancing methane-tin contact surface, thus improving heat transfer. That could be achieved by using porous devices such as gas spargers to break bubbles into smaller ones.

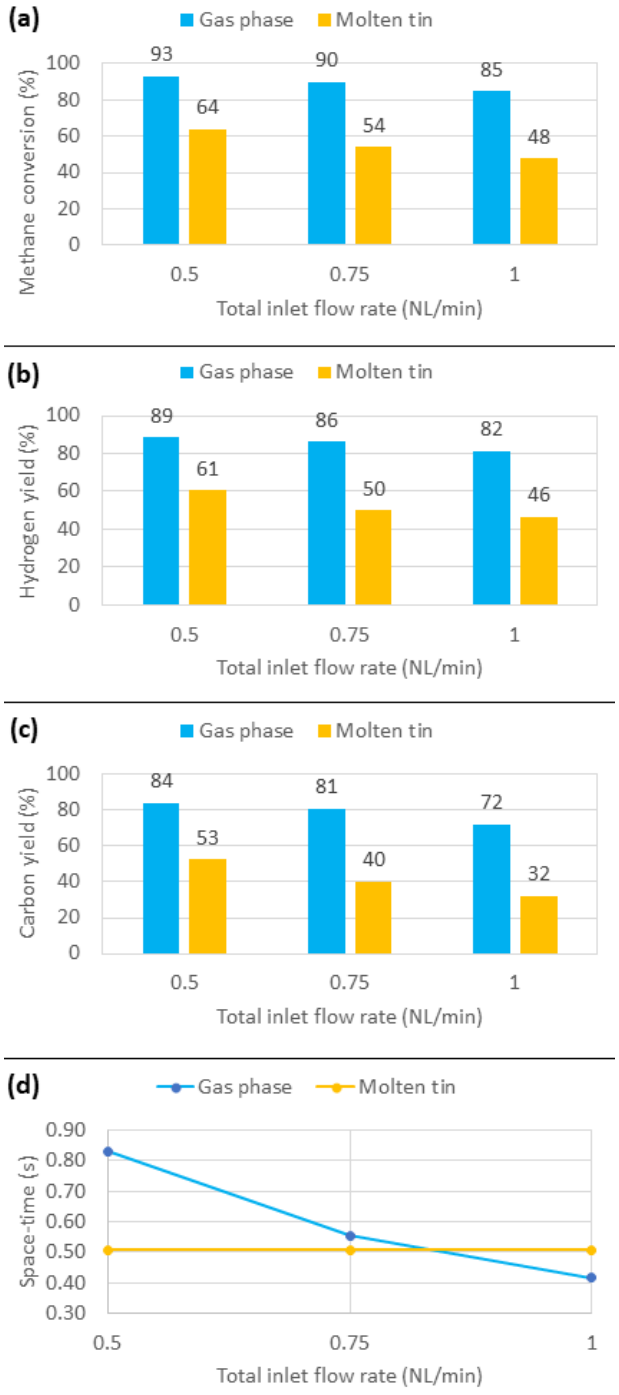

Figure 9: Total inlet flow rate effect on methane pyrolysis in gas phase and in liquid tin with a fixed methane molar fraction of 0.3 and a constant temperature of 1300°C: (a) methane conversion, (b) hydrogen yield, (c) carbon yield, (d) gas space-time in the hot zone of the reactor.

4.3 Effect of methane molar fraction

For both routes, when fixing the total feed rate (0.5 NL/min) and increasing methane molar fraction $y_{0,CH4}$ (0.1-0.3-0.5) at different temperatures, methane conversion generally tended to decrease, while hydrogen and carbon yields did not vary significantly (Figures 10 and 11). For example, when $y_{0,CH4}$ increased from 0.1 to 0.5 for gas-phase pyrolysis at 1300°C, X_{CH4} decreased from 95% to 91%, Y_C remained stable at around 81%, while Y_{H2} decreased from 93% to 89%. For molten tin at 1300°C, there was an insignificant change, X_{CH4} decreased from 65% to 64%, Y_C decreased from 53% to 52%, while Y_{H2} decreased from 63% to 62%.

This behavior was less significant when T approached 1400 °C because methane decomposition was almost 100%.

Increasing methane molar fraction in the inlet feed may have increased the reaction rate, which is directly proportional to methane concentration (Eq. 17) [49]. However, this also led to more chemical expansion, which reduced the space-time. It is possible that the effect of the space-time decrease overcame the effect of the reaction rate increase, which yielded lower methane conversion at higher methane inlet fractions.

Rodat et al. [50] found that increasing methane inlet fraction from 0.10 to 0.36 decreased hydrogen yield from 83% to 74%, following the same behavior as methane conversion. The methane decomposition mechanism may help for a better understanding of such results. The most agreed mechanism up to date claims that methane decomposes as follows [49]:

$$CH_4 \rightarrow CH_3^* + H^* \quad (20)$$
$$CH_3^* \rightarrow CH_2^* + H^* \quad (21)$$
$$CH_2^* \rightarrow CH^* + H^* \quad (22)$$
$$CH^* \rightarrow C + H^* \quad (23)$$

Hydrogen could then form by interaction of any two hydrogen radicals:

$$2H^* \rightarrow H_2 \quad (24)$$

According to this mechanism, solid carbon could not be formed if the methane molecule did not yet lose all its hydrogen atoms. In other words, carbon formation is the latest step in methane decomposition, and hence, lower methane conversion leads to lower carbon yields. In contrast, hydrogen can be formed during uncomplete methane decomposition in parallel with secondary hydrocarbons production. This mechanism suggests that hydrogen yield behavior may not exactly follow methane conversion and carbon yield evolution when increasing methane inlet fraction.

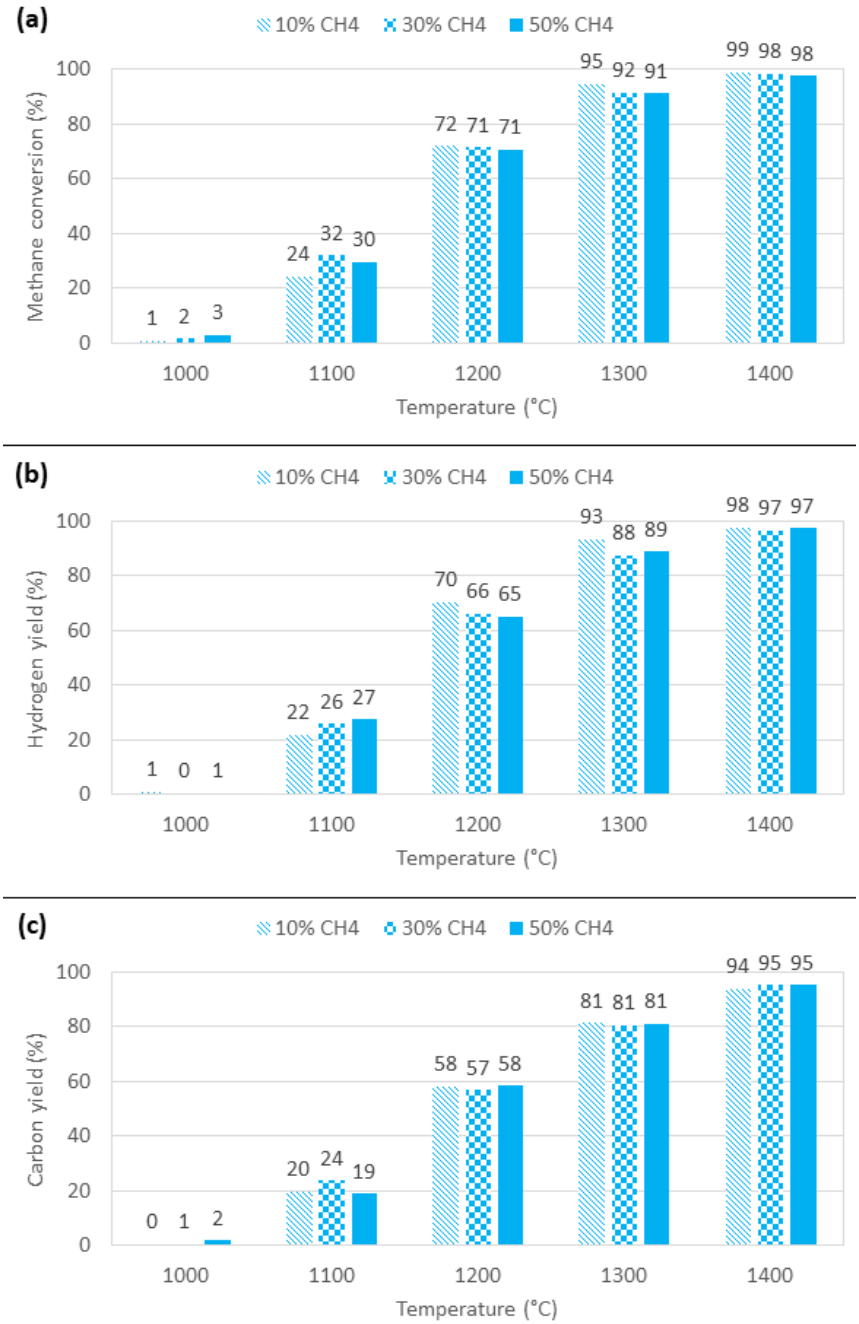

Figure 10: Effect of methane molar fraction on methane conversion and products yields in gas-phase methane pyrolysis: (a) methane conversion, (b) hydrogen yield, (c) carbon yield.

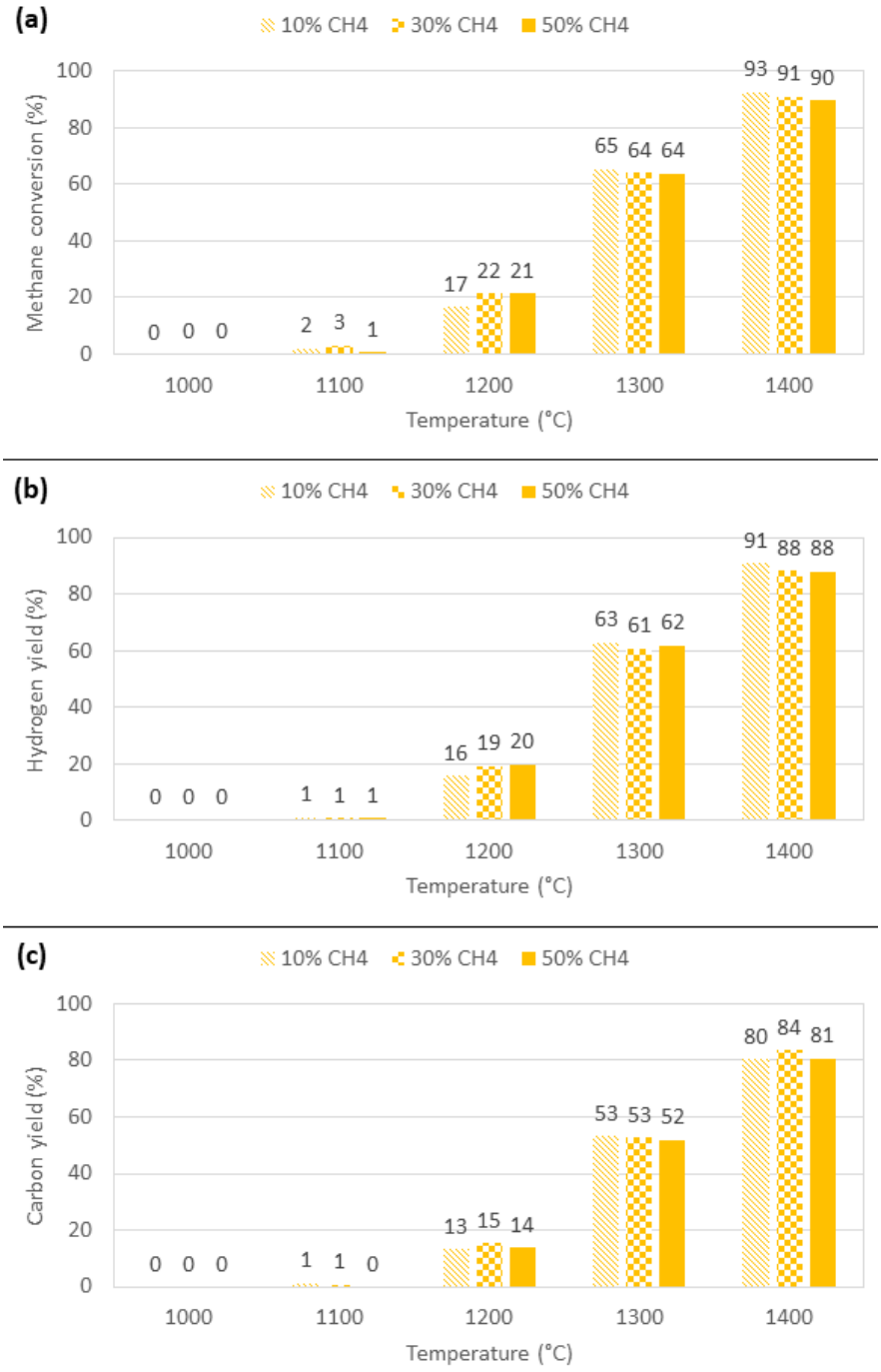

Figure 11: Effect of methane molar fraction on methane conversion and products yields in molten-tin methane pyrolysis: (a) methane conversion, (b) hydrogen yield, (c) carbon yield.

4.4 Energy efficiencies

The solar-to-fuel efficiency describes to which extent the solar power input was exploited to generate fuels. η_{SF} rose with increasing methane inlet fraction at a fixed temperature (Figure 12). For example, when increasing methane inlet fraction from 0.1 to 0.5 at 1200°C, η_{SF} increased from 1.3% to 5.5% and from 0.2% to 1.6% for gas-phase and molten-tin methane pyrolysis, respectively. The maximum η_{SF} for gas-phase methane pyrolysis was 6.2% at 1300°C, against 4.5% for molten tin at 1400°C.

The thermal efficiency of the reactor $\eta_{thermal}$ followed the same tendency with increasing methane inlet molar fraction. At 1200°C, for example, it increased from 0.8% to 3.8% for gas

phase and from 0.4% to 1.8% for molten tin when $y_{0,CH4}$ was increased from 0.1 to 0.5. $\eta_{thermal}$ followed the same trend as η_{SF}, with maximum values reached for the same runs (maximum $\eta_{thermal}$ of 4.4% at 1300°C for gas-phase methane pyrolysis and 3.3% at 1400°C for molten tin).

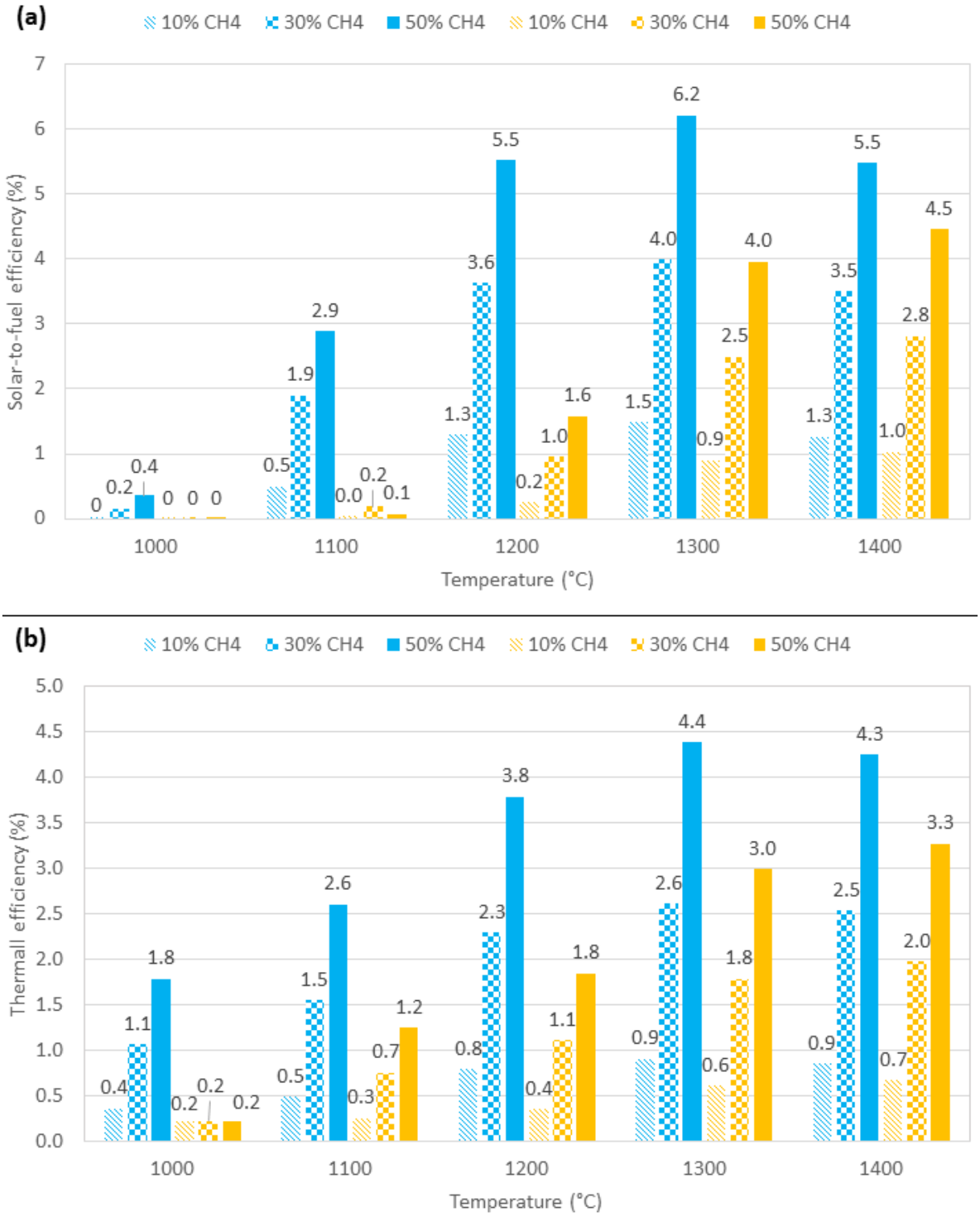

Figure 12: Solar-to-fuel and thermal efficiencies for pyrolysis in gas-phase (blue color) and molten-tin (orange color) configurations.

5 Carbon product analysis

5.1 Morphological analysis

Carbon samples produced from both routes and collected in the filtering device were analyzed through scanning electron microscopy (SEM) (HITACHI S4800) to determine the morphology of the material. SEM images of carbon produced in gas-phase configuration (Figure 13) show stacked granular carbon particles with spherical shapes (primary size ~50-100 nm). In contrast, SEM images of carbon produced in molten tin reveal a sheet-like morphology (Figure 14). This morphology seems to be often encountered for pyrolysis in molten media [36,40]. This may be due to the bubbling configuration implying that carbon particles were formed in a bubble preferably at the liquid-gas interface. Methane decomposition likely took place at the gas-tin surface contact, which probably led to the formation of spherical sheets of carbon. Once the bubbles broke up on the top surface of the tin bath, flat sheets were overlaid. However, on the sheet-like structure, small quantities of spread carbon particles (size below 50 nm) can be observed, probably arising from gas-phase decomposition in the bubbles volume.

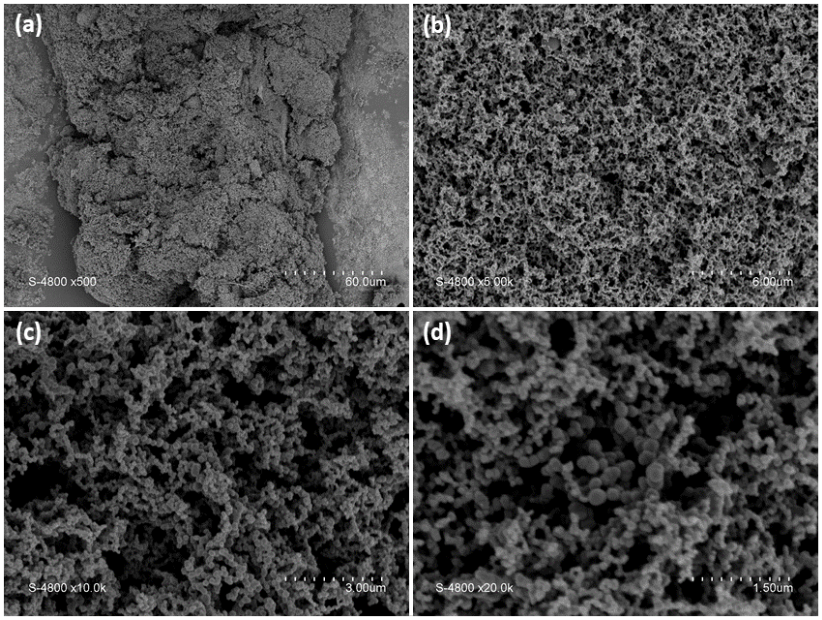

Figure 13: (a) SEM image of carbon sample produced in gas-phase methane pyrolysis. Images (b), (c), and (d) are gradual zoom as follows: (b) scale of (a)/10, (c) scale of (a)/20, (d) scale of (a)/40.

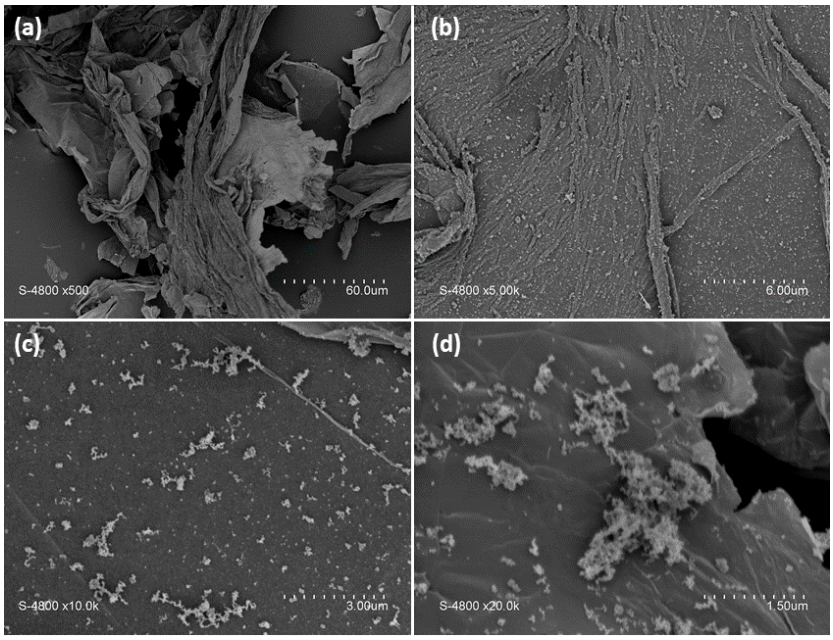

Figure 14: (a) SEM image of carbon sample produced during methane pyrolysis in molten tin. Images (b), (c), and (d) are gradual zoom as follows: (b) scale of (a)/10, (c) scale of (a)/20, (d) scale of (a)/40.

5.2 Elemental composition analysis

Energy dispersive X-Ray analysis (EDX) (Oxford Instruments X-Max N SDD) was performed for carbon sample from molten tin pyrolysis to determine carbon tin-contamination levels. The presence of tin dispersed particles can be confirmed by the bright zones in Figure 15. These traces of tin result from droplets entrainment by the gas flow and their subsequent recovery in the carbon product. Analysis was done at different brightened zones, as shown in Figure 15. Quantitative results are shown in Table 5. Zones with the highest tin contamination were zones 12 and 13, with 40.84 wt% and 78.43 wt% Sn content inside, respectively. In contrast, zone 9 showed only 3.32 wt% Sn content. The selected analyzed zones also showed a weak oxygen content: zones 10 and 13 had the highest oxygen content with 11.2% and 8.13%, respectively. Although there was a precaution to avoid tin metal oxidation, it probably occurred during the startup and shutdown of the process. Moreover, solid tin was stored for a long time period before experiments, which could have resulted in partial tin oxidation that may explain some of the oxygen presence in the collected carbon. The presence of some tin contamination in the collected carbon is obvious. However, tin-contamination levels can be reduced and were mostly due to the agitation of the bath and tin entrainment when inlet gas feed reached relatively high values (1 NL/min).

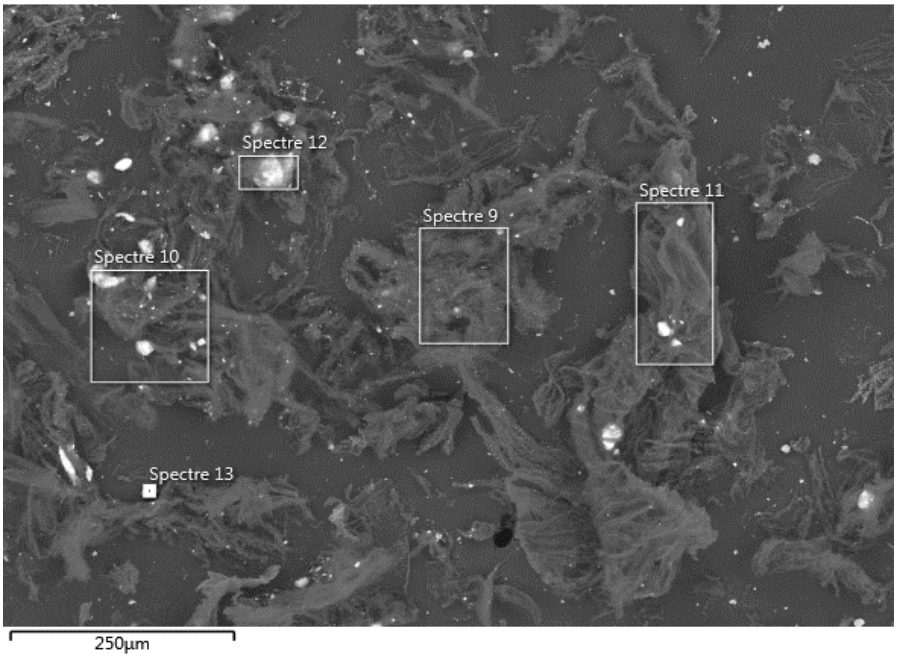

Figure 15: Electronic image of the carbon sample produced during pyrolysis in molten tin.

Table 5: EDX analytical results for tin-contamination at different zones of the carbon specimen

Zone N°	C (wt%)	O (wt%)	Sn (wt%)	Total (%)
9	90.08	6.59	3.32	99.99
10	78.14	11.2	10.66	100
11	89.57	4.22	6.21	100
12	56.45	2.71	40.84	100
13	13.44	8.13	78.43	100

5.3 X-ray diffraction analysis

Structural analysis of carbon samples was done by X-ray diffraction (XRD) (Malvern Panalytical X'Pert PRO). Results are shown in Figure 16. In gas phase, broad peaks indicated the presence of small particles of amorphous carbon black [54]. Using Scherrer equation Eq. (25), the average crystallite size was estimated to be 1.8 nm. Scherrer equation is given as follows:

$$D = \frac{K.\lambda}{\beta.cos\theta} \tag{25}$$

where D is the mean size of the ordered crystalline domains, K is a dimensionless shape factor (0.9), λ is X-ray wavelength, β is the broadening at half the maximum intensity (rad) and θ is the Bragg angle (rad).

XRD of carbon produced in molten tin revealed the formation of graphitic carbon with 2.5 nm crystalline size calculated using Eq. (25) and a high Sn presence through the narrow peaks with high intensity. In addition, peaks of SnO_2 were also identified, confirming the presence of oxygen as evidenced by EDX analysis. The presence of stannic oxide could be minimized by shortening the startup and the shutdown operations.

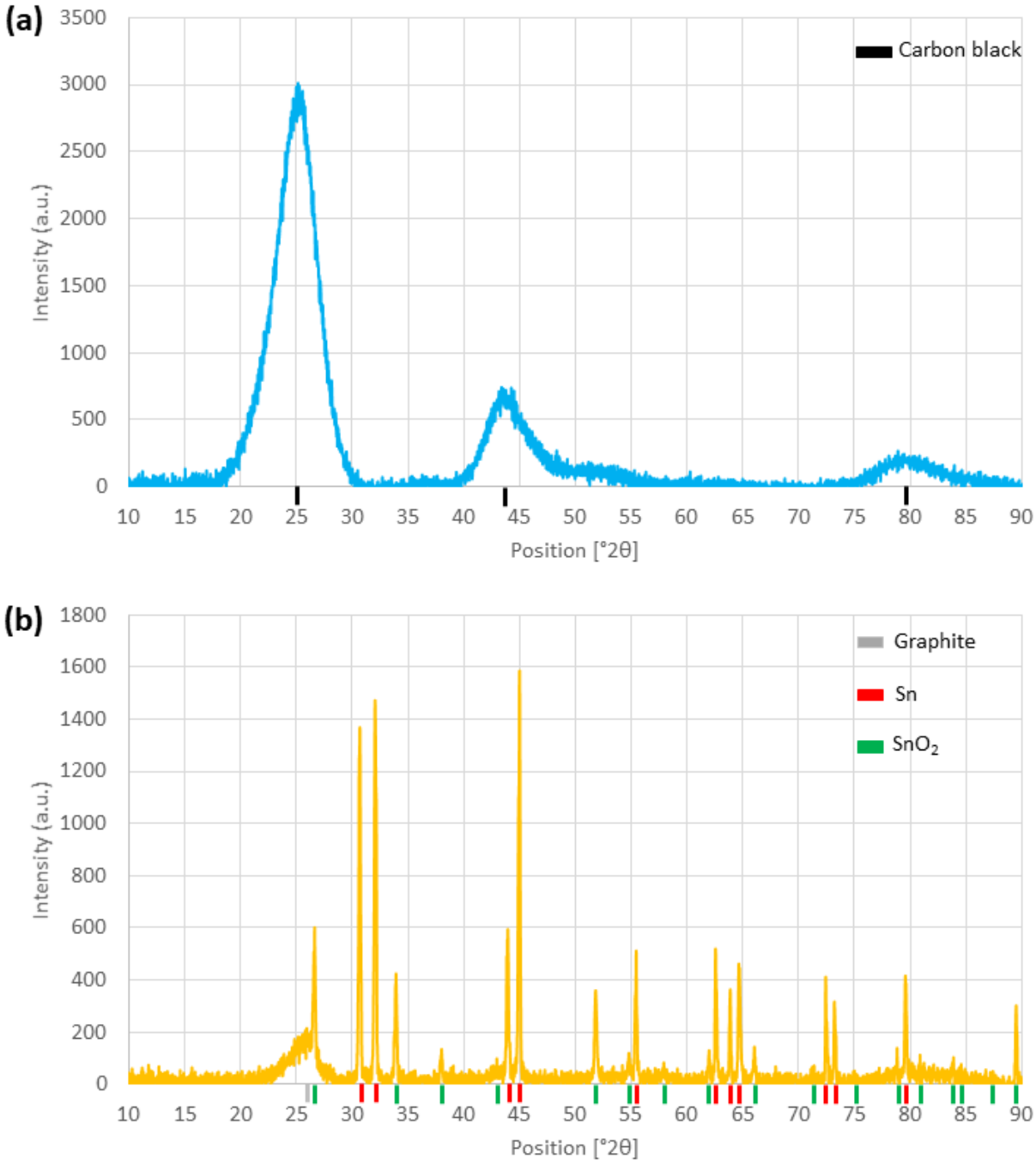

Figure 16: XRD analysis of carbon samples for pyrolysis in (a) gas phase, (b) molten tin.

6 Conclusions

Solar methane pyrolysis in molten media is a promising path for CO_2-free hydrogen production. By bubbling methane in a hot liquid metal bath, heat transfer is improved, and reactor clogging is avoided due to carbon flotation atop the free surface of the liquid due to density difference with metals. A performance comparison between uncatalyzed gas-phase and molten-tin (liquid bath height = 120 mm) methane pyrolysis was thus conducted.

For both routes, rising the temperature increased methane conversion and products yield. When the temperature was increased from 1000°C to 1400°C, X_{CH4} increased from 2% to 98% and from 0% to 91% for gas-phase and molten-tin methane pyrolysis, respectively.

Increasing the inlet gas flow rate (0.5-0.75-1 NL/min) at a fixed methane inlet fraction (0.3) and a fixed temperature (1300°C) decreased methane conversion and products yield since it decreased gas space-time in the reactor (e.g., when the inlet feed was doubled to 1 NL/min, X_{CH4} decreased from 93% to 85% and from 64% to 48% for gas-phase and molten-tin methane pyrolysis, respectively). Theoretically, the inlet gas feed affected space-time significantly only in the gas phase (0.83-0.42 s). In molten tin, it only affected bubbles formation time (0.008 s with D_b = 5.19 mm), which was considered negligible compared to bubbles rising time (0.5 s). However, this would be true only if there was no coalescence between bubbles, which was probably not the case experimentally.

Increasing methane inlet fraction (0.1-0.5), with a fixed total gas flow rate (0.5 NL/min), generally decreased methane conversion (gas phase at 1300°C: X_{CH4} = 95-91%, molten tin at 1300°C: X_{CH4} = 65-64%).

Regarding the effect of the medium type on pyrolysis, results showed lower conversion and products yield in molten tin than in gas phase for all temperatures (1000-1400°C), chiefly due to lower gas space-time. In molten tin, large bubbles (reduced contact area for heat transfer), inducing lower bubble rising time (reduced liquid/gas contact time) and possibly coalescence phenomenon, explained the lower methane conversion. Generating smaller bubbles (<1 mm diameter) would enhance space-time in molten tin (0.83 s at 1300°C with Q_0 = 0.5 NL/min equivalent to the space-time in gas-phase pyrolysis). Moreover, the gas-liquid interfacial area would further increase by a factor of 5.2, which would additionally boost heat transfer. In such conditions, the benefits of pyrolysis in molten metal could be unveiled, besides the intrinsic advantage of much easier downstream carbon separation.

Carbon byproduct is important to minimize hydrogen production costs on the way to process scale-up. Carbon produced in gas-phase pyrolysis was carbon black powder (with 50-100 nm average size). In contrast, carbon produced during pyrolysis in molten tin had a sheet-like morphology with some carbon black spread on the sheets, probably formed from gas-phase pyrolysis inside bubbles.

In future works, mixtures of Sn and an active metal (e.g., Ni, Fe) or metal alloys could be used to increase kinetics and boost conversion. Indeed, tin is a non-catalytic metal and it is expected that catalytically active alloys (such as Cu-Bi) would favor liquid phase pyrolysis with high methane conversion and no catalyst deactivation as carbon should float on top of the liquid phase. Moreover, generating small bubbles could further improve heat transfer (higher gas-liquid surface contact) and increase the rising time in the hot bath. This could be obtained through a smaller feeder diameter or gas spargers. Further work is also required for a better understanding of the various reaction mechanisms in bubbling regime, with dedicated multiphase system modelling from bubble to reactor scale.

Author Contributions: Methodology, Validation, Formal analysis, Investigation, Data curation, M.M., S.R., and S.A.; Writing—original draft preparation, M.M.; writing—review and editing, M.M., S.R., and S.A.; supervision, S.R. and S.A.; project administration, S.R. and

S.A.; funding acquisition, S.R. and S.A. All authors have read and agreed to the published version of the manuscript.

Conflicts of Interest: The authors declare no conflicts of interest

Acknowledgements
This work was partially supported by the French ‘‘Investments for the future” program managed by the National Agency for Research, under contract ANR-10-LABX-22-01 (Labex SOLSTICE). The authors thank Roger Garcia (PROMES-CNRS) for his support in the design and installation of the solar reactor, Régis Rodriguez and Emmanuel Guillot for their support to set the data acquisition system, and Eric Bêche for XRD analysis.

References

[1] LIOR N. Energy resources and use: The present situation and possible paths to the future☆. Energy 2008;33:842–57. https://doi.org/10.1016/j.energy.2007.09.009.

[2] Hydrogen Industry Applications: Past, Present, and Future. 2022. https://wha-international.com/hydrogen-in-industry/ (accessed January 28, 2022).

[3] Garcia G, Arriola E, Chen W-H, De Luna MD. A comprehensive review of hydrogen production from methanol thermochemical conversion for sustainability. Energy 2021;217:119384. https://doi.org/10.1016/j.energy.2020.119384.

[4] Aydin MI, Dincer I. An assessment study on various clean hydrogen production methods. Energy 2022;245:123090. https://doi.org/10.1016/j.energy.2021.123090.

[5] Plevan M, Geißler T, Abánades A, Mehravaran K, Rathnam RK, Rubbia C, et al. Thermal cracking of methane in a liquid metal bubble column reactor: Experiments and kinetic analysis. Int J Hydrogen Energy 2015;40:8020–33. https://doi.org/10.1016/j.ijhydene.2015.04.062.

[6] Cai L, He T, Xiang Y, Guan Y. Study on the reaction pathways of steam methane reforming for H2 production. Energy 2020;207:118296. https://doi.org/10.1016/j.energy.2020.118296.

[7] Chein R-Y, Lu C-Y, Chen W-H. Syngas production via chemical looping reforming using methane-based feed and NiO/Al2O3 oxygen carrier. Energy 2022;250:123815. https://doi.org/10.1016/j.energy.2022.123815.

[8] Wang F, Shi X, Zhang C, Cheng Z, Chen X. Effects of non-uniform porosity on thermochemical performance of solar driven methane reforming. Energy 2020;191:116575. https://doi.org/10.1016/j.energy.2019.116575.

[9] Lemus RG, Martínez Duart JM. Updated hydrogen production costs and parities for conventional and renewable technologies. Int J Hydrogen Energy 2010;35:3929–36. https://doi.org/10.1016/j.ijhydene.2010.02.034.

[10] Pashchenko D, Makarov I. Carbon deposition in steam methane reforming over a Ni-based catalyst: Experimental and thermodynamic analysis. Energy 2021;222:119993. https://doi.org/10.1016/j.energy.2021.119993.

[11] Carbon Black Market - Growth, Trends, COVID-19 Impact, and Forecasts (2022 - 2027) n.d. https://www.mordorintelligence.com/industry-reports/carbon-black-market (accessed January 28, 2022).

[12] Dagle RA, Dagle V, Bearden MD, Holladay JD, Krause TR, Ahmed S. An Overview of Natural Gas Conversion Technologies for Co-Production of Hydrogen and Value-Added Solid Carbon Products. Pacific Northwest National Lab: Richland, WA, USA: 2017. https://doi.org/10.2172/1411934.

[13] Abanades S, Flamant G. Hydrogen production from solar thermal dissociation of methane in a high-temperature fluid-wall chemical reactor. Chem Eng Process Process Intensif 2008;47:490–8. https://doi.org/10.1016/j.cep.2007.01.006.

[14] Rodat S, Abanades S, Coulié J, Flamant G. Kinetic modelling of methane decomposition in a tubular solar reactor. Chem Eng J 2009;146:120–7. https://doi.org/10.1016/j.cej.2008.09.008.

[15] Rodat S, Abanades S, Flamant G. Experimental evaluation of indirect heating tubular reactors for solar methane pyrolysis. Int J Chem React Eng 2010;8. https://doi.org/10.2202/1542-6580.2084.

[16] Abánades A, Rubbia C, Salmieri D. Technological challenges for industrial development of hydrogen production based on methane cracking. Energy 2012;46:359–63. https://doi.org/10.1016/j.energy.2012.08.015.

[17] Rodat S, Abanades S. A Hybrid Windowless Dual Tube Solar Reactor for Continuous Volumetric Natural Gas Dissociation. Front Energy Res 2020;8. https://doi.org/10.3389/fenrg.2020.00206.

[18] Rodat S, Abanades S, Boujjat H, Chuayboon S. On the path toward day and night continuous solar high temperature thermochemical processes: A review. Renew Sustain Energy Rev 2020;132. https://doi.org/10.1016/j.rser.2020.110061.

[19] Abanades S, Flamant G. Experimental study and modeling of a high-temperature solar chemical reactor for hydrogen production from methane cracking. Int J Hydrogen Energy 2007;32:1508–15. https://doi.org/10.1016/j.ijhydene.2006.10.038.

[20] Ozalp N, Ibrik K, Al-Meer M. Kinetics and heat transfer analysis of carbon catalyzed solar cracking process. Energy 2013;55:74–81. https://doi.org/10.1016/j.energy.2013.02.022.

[21] Chen J, Li Y, Li Z, Zhang X. Production of COx-free hydrogen and nanocarbon by direct decomposition of undiluted methane on Ni-Cu-alumina catalysts. Appl Catal A Gen 2004;269:179–86. https://doi.org/10.1016/j.apcata.2004.04.016.

[22] Abbas HF, Wan Daud WMA. Hydrogen production by methane decomposition: A review. Int J Hydrogen Energy 2010;35:1160–90. https://doi.org/10.1016/j.ijhydene.2009.11.036.

[23] Patel S, Kundu S, Halder P, Marzbali MH, Chiang K, Surapaneni A, et al. Production of hydrogen by catalytic methane decomposition using biochar and activated char produced from biosolids pyrolysis. Int J Hydrogen Energy 2020;45:29978–92. https://doi.org/10.1016/j.ijhydene.2020.08.036.

[24] Abanades S, Kimura H, Otsuka H. Kinetic investigation of carbon-catalyzed methane decomposition in a thermogravimetric solar reactor. Int J Hydrogen Energy 2015;40:10744–55. https://doi.org/10.1016/j.ijhydene.2015.07.023.

[25] Tyrer D. “Production of hydrogen” U.S. Patent 1 803 221, Apr. 28,. The United States Patent Office. 1803221, 1931. https://doi.org/10.1126/science.53.1377.481.

[26] Msheik M, Rodat S, Abanades S. Methane Cracking for Hydrogen Production: A Review of Catalytic and Molten Media Pyrolysis. Energies 2021;14:3107. https://doi.org/10.3390/en14113107.

[27] Upham DC, Agarwal V, Khechfe A, Snodgrass ZR, Gordon MJ, Metiu H, et al. Catalytic molten metals for the direct conversion of methane to hydrogen and separable carbon. Science (80-) 2017;358:917–21. https://doi.org/10.1126/science.aao5023.

[28] Farmer TC, McFarland EW, Doherty MF. Membrane bubble column reactor model for the production of hydrogen by methane pyrolysis. Int J Hydrogen Energy 2019;44:14721–31. https://doi.org/10.1016/j.ijhydene.2019.03.023.

[29] Palmer C, Tarazkar M, Kristoffersen HH, Gelinas J, Gordon MJ, McFarland EW, et al. Methane Pyrolysis with a Molten Cu-Bi Alloy Catalyst. ACS Catal 2019;9:8337–45. https://doi.org/10.1021/acscatal.9b01833.

[30] Zeng J, Tarazkar M, Pennebaker T, Gordon MJ, Metiu H, McFarland EW. Catalytic Methane Pyrolysis with Liquid and Vapor Phase Tellurium. ACS Catal 2020;10:8223–30. https://doi.org/10.1021/acscatal.0c00805.

[31] Leal Pérez BJ, Medrano Jiménez JA, Bhardwaj R, Goetheer E, van Sint Annaland M, Gallucci F. Methane pyrolysis in a molten gallium bubble column reactor for sustainable hydrogen production: Proof of concept & techno-economic assessment. Int J Hydrogen Energy 2020. https://doi.org/10.1016/j.ijhydene.2020.11.079.

[32] Wang K, Li WS, Zhou XP. Hydrogen generation by direct decomposition of hydrocarbons over molten magnesium. J Mol Catal A Chem 2008;283:153–7. https://doi.org/10.1016/j.molcata.2007.12.018.

[33] Serban M, Lewis MA, Marshall CL, Doctor RD. Hydrogen production by direct contact pyrolysis of natural gas. Energy and Fuels 2003;17:705–13. https://doi.org/10.1021/ef020271q.

[34] Geißler T, Plevan M, Abánades A, Heinzel A, Mehravaran K, Rathnam RK, et al. Experimental investigation and thermo-chemical modeling of methane pyrolysis in a liquid metal bubble column reactor with a packed bed. Int J Hydrogen Energy 2015;40:14134–46. https://doi.org/10.1016/j.ijhydene.2015.08.102.

[35] Zaghloul N, Kodama S, Sekiguchi H. Hydrogen Production by Methane Pyrolysis in a Molten-Metal Bubble Column. Chem Eng Technol 2021;44:1986–93. https://doi.org/10.1002/ceat.202100210.

[36] Kang D, Rahimi N, Gordon MJ, Metiu H, McFarland EW. Catalytic methane pyrolysis in molten MnCl2-KCl. Appl Catal B Environ 2019;254:659–66. https://doi.org/10.1016/j.apcatb.2019.05.026.

[37] Kang D, Palmer C, Mannini D, Rahimi N, Gordon MJ, Metiu H, et al. Catalytic Methane Pyrolysis in Molten Alkali Chloride Salts Containing Iron. ACS Catal 2020;10:7032–42. https://doi.org/10.1021/acscatal.0c01262.

[38] Parkinson B, Patzschke CF, Nikolis D, Raman S, Dankworth DC, Hellgardt K. Methane pyrolysis in monovalent alkali halide salts: Kinetics and pyrolytic carbon properties. Int J Hydrogen Energy 2021;46:6225–38. https://doi.org/10.1016/j.ijhydene.2020.11.150.

[39] Patzschke CF, Parkinson B, Willis JJ, Nandi P, Love AM, Raman S, et al. Co-Mn catalysts for H 2 production via methane pyrolysis in molten salts. Chem Eng J 2021;414:128730. https://doi.org/10.1016/j.cej.2021.128730.

[40] Rahimi N, Kang D, Gelinas J, Menon A, Gordon MJ, Metiu H, et al. Solid carbon production and recovery from high temperature methane pyrolysis in bubble columns containing molten metals and molten salts. Carbon N Y 2019;151:181–91. https://doi.org/10.1016/j.carbon.2019.05.041.

[41] Alchagirov BB, Chochaeva AM. Temperature dependence of the density of liquid tin. High Temp 2000;38:44–8. https://doi.org/10.1007/BF02755565.

[42] Paxman D, Trottier S, Nikoo M, Secanell M, Ordorica-Garcia G. Initial Experimental and Theoretical Investigation of Solar Molten Media Methane Cracking for Hydrogen Production. Energy Procedia 2014;49:2027–36. https://doi.org/10.1016/j.egypro.2014.03.215.

[43] Lee J, Shimoda W, Tanaka T. Surface Tension and its Temperature Coefficient of Liquid Sn-X (X=Ag, Cu) Alloys. Mater Trans 2004;45:2864–70. https://doi.org/10.2320/matertrans.45.2864.

[44] Andreini RJ, Foster JS, Callen RW. Characterization of gas bubbles injected into molten metals under laminar flow conditions. Metall Trans B 1977;8:625–31. https://doi.org/10.1007/BF02669340.

[45] Muhich CL, Blaser S, Hoes MC, Steinfeld A. Comparing the solar-to-fuel energy conversion efficiency of ceria and perovskite based thermochemical redox cycles for splitting H2O and CO2. Int J Hydrogen Energy 2018;43:18814–31. https://doi.org/10.1016/j.ijhydene.2018.08.137.

[46] Goodwin DG, Speth RL, Moffat HK, Weber BW. Cantera: An object-oriented software toolkit for chemical kinetics, thermodynamics, and transport processes. Version 2.5.1, 2021. Available online: https://www.cantera.org (accessed on 15 January 2021) n.d.

[47] Bulfin B, Miranda M, Steinfeld A. Performance Indicators for Benchmarking Solar Thermochemical Fuel Processes and Reactors. Front Energy Res 2021;9. https://doi.org/10.3389/fenrg.2021.677980.

[48] Rodat S. Production d'hydrogène et de noirs de carbone par décomposition thermique de gaz naturel dans des réacteurs solaires. UPVD. 2010.

[49] Sánchez-Bastardo N, Schlögl R, Ruland H. Methane Pyrolysis for CO2-Free H2 Production: A Green Process to Overcome Renewable Energies Unsteadiness. Chemie-Ingenieur-Technik 2020;92:1596–609. https://doi.org/10.1002/cite.202000029.

[50] Rodat S, Abanades S, Flamant G. High-Temperature Solar Methane Dissociation in a Multitubular Cavity-Type Reactor in the Temperature Range 1823−2073 K. Energy & Fuels 2009;23:2666–74. https://doi.org/10.1021/ef900037v.

[51] Sajid MU, Bicer Y. Thermodynamic assessment of chemical looping combustion and solar thermal methane cracking-based integrated system for green ammonia production. Therm Sci Eng Prog 2020;19:100588. https://doi.org/10.1016/j.tsep.2020.100588.

[52] Gonzalez-Aguilar J, Dème I, Fulcheri L, Flamant G, Gruenberger TM, Ravary B. Comparison of simple particle-radiation coupling models applied on a plasma black process. Plasma Chem Plasma Process 2004;24:603–23. https://doi.org/10.1007/s11090-004-7935-5.

[53] Holmen A, Olsvik O, Rokstad OA. Pyrolysis of natural gas: chemistry and process concepts. Fuel Process Technol 1995;42:249–67. https://doi.org/10.1016/0378-3820(94)00109-7.

[54] Li ZQ, Lu CJ, Xia ZP, Zhou Y, Luo Z. X-ray diffraction patterns of graphite and turbostratic carbon. Carbon N Y 2007;45:1686–95. https://doi.org/10.1016/j.carbon.2007.03.038.